PAPER

Check for updates

First-principles study of M_4AlC_3 (M = Ti, Zr) MAX phases under hydrostatic pressure: material design for industrial applications

Ananya Basak,[a] Ahmad Irfan,[bc] Mst. Asma Khatun,[d] M. M. Rabbi,[e] Disha Roy,[a] Mohammad Yasin Hayat Khan,[f] M. S. Ali,[a] Md. Ferdous Rahman [ID][g] and Md. Atikur Rahman [ID] *[a]

MAX phase compounds, combining metallic and ceramic properties, are ideal for high-pressure environments due to their excellent electrical and thermal conductivity, corrosion and oxidation resistance, and damage tolerance. This study investigates the structural, mechanical, electronic, thermal, and optical properties of M_4AlC_3 (M = Ti, Zr) under hydrostatic pressure. Negative formation energies and positive phonon dispersion confirm thermodynamic and dynamic stability, while mechanical stability aligns with Born's criteria. Increasing stiffness constants and moduli (bulk, shear, Young's), along with Poisson's and Pugh's ratios, suggest enhanced mechanical performance. Ti_4AlC_3 and Zr_4AlC_3 are brittle below 60 GPa and 40 GPa, respectively, but become ductile above these pressures. A rising machinability index with pressure supports industrial applicability. Anisotropy is confirmed *via* 3D plots, and DOS analysis reveals metallic nature. Strong UV absorption and conductivity highlight their potential in UV-optical devices. Reflectivity above 60% and high IR reflectance suggest use in thermal coatings and solar heat management. Increasing Debye and melting temperatures under pressure further indicate their suitability for high-temperature applications. These findings support their use in extreme conditions such as aerospace, deep-sea exploration, and ultra-hard ceramic development.

1. Introduction

MAX phases have recently attracted significant interest from materials scientists due to their unique combination of chemical, physical, electrical, and mechanical properties. Composed mainly of carbides and nitrides, these compounds follow the general formula $M_{n+1}AX_n$ (n = 1, 2, 3…), where M is a transition metal, A is an element from groups IIA or IVA, and X is carbon or nitrogen. They crystallize in a layered hexagonal structure with $P6_3/mmc$ symmetry.[1] MAX phases are uniquely blend metallic and ceramic characteristics. While metals typically offer high thermal and electrical conductivity, plastic deformability, and thermal shock resistance, ceramics provide high stiffness, excellent high-temperature performance, and superior resistance to corrosion and oxidation. MAX phases combine these features, earning the term "metallic ceramics" in literature.[2–8] Because of these exceptional properties, they are suitable for demanding applications such as gas burner nozzles, high-temperature foil bearings, and heating elements. In high-temperature conditions, they serve as alternatives to graphite and are used in tools for dry concrete drilling and various industrial roles.[9] Their rising prominence stems from potential uses in advanced technologies including sensors, high-temperature ceramics, electrical contacts, catalytic systems, and protective coatings. Consequently, MAX phases have become a major focus in materials research.[9,10] Some MAX phase compounds are applicable to nuclear technology, for example, Ti_3AlC_2 and Ti_3SiC_2, are found to be resistant to radiation damage.[11] First documented by Nowotny *et al.* in the 1960s, around 100 ternary nitrides and carbides have been identified.[12] MAX phases are generally grouped based on the integer n into M_2AX (211), M_3AX_2 (312), and M_4AX_3 (413) types,[13–15] with examples including Ti_2AlC and Ti_2AlN (211), Ti_3AlC_2 and Ti_2GeC_2 (312), and Ti_4AlN_3 and Nb_4AlC_3 (413). Other variants like Ti_5SiC_4 (514), Ta_6AlC_5 (615), and Ti_7SnC_6 (716) also exist. Differences among these subgroups arise from

[a]Department of Physics, Pabna University of Science and Technology, Pabna-6600, Bangladesh. E-mail: atik0707phy@gmail.com

[b]Central Labs, King Khalid University, AlQura'a, P.O. Box 960, Abha, Saudi Arabia

[c]Department of Chemistry, College of Science, King Khalid University, P.O. Box 9004, Abha 61413, Saudi Arabia

[d]Department of Physics, Hajee Mohammad Danesh Science and Technology University, Dinajpur-5200, Bangladesh

[e]Department of Physics, University of Rajshahi, Rajshahi-6205, Bangladesh

[f]Department of Electrical and Electronic Engineering, International Islamic University Chittagong, Kumira, Chittagong, 4318, Bangladesh

[g]Advanced Energy Materials and Solar Cell Research Laboratory, Department of Electrical and Electronic Engineering, Begum Rokeya University, Rangpur 5400, Bangladesh

variations in M-layer stacking, resulting in distinct structural features.[16–19]

The MAX phase materials have been first synthesized in the 1960s belonged to the 211 family.[20] However, significant advancements began in the mid-1990s when Barsoum and collaborators highlighted their high-temperature stability combined with excellent machinability. Since then, extensive studies have focused on their synthesis and properties, including the impact of pressure on their structural, elastic, electrical, optical, and thermodynamic behaviors.[21–25] However, compared to the huge studies on 211 and 312 MAX phases, relatively limited work has been published on the 413 MAX phases. In 2000, the first 413 MAX phase, Ti_4AlN_3, was discovered which play significant role in the exploration of these type materials.[6] Though there is a relatively small amount of research on, the unique properties and potential applications of 413 MAX phases still attract interest. Ti_4SiC_3 and Ti_4GeC_3 are highlighted by their excellent resistance to oxidation and corrosion which make them highly effective as protective coatings in thin film technology. These materials are particularly useful in environments where resistance to oxidized chemicals and high temperatures is essential.[25–27] On the other hand, materials like Ta_4AlC_3, Nb_4AlC_3, Ti_4AlN_3, and V_4AlC_3 are usually used in bulk form due to their excellent damage tolerance and mechanical properties. These MAX phases also exhibit high resistance to fracture and wear which makes them suitable for applications in such an environment where durability is critical. For instance, they are good in high-temperature applications, structural components in high-stress systems and other applications where materials should survive under repeated mechanical stresses and thermal shocks.[27–31] Li, Z., Zhang *et al.* studied the physical properties of MAX phase's materials Ti_2AlC and Cr_2AlC used for highly dense passivation enhanced corrosion resistance and coatings for ATF.[32,33] Hu *et al.* contribute to the family of 413 MAX phases by identifying Nb_4AlC_3. Studies revealed that Nb_4AlC_3 has same hexagonal layered crystal structure as Ti_4AlN_3. Nb_4AlC_3 exhibit high-temperature stability, damage tolerance and high resistance to oxidation, which make it suitable for various industrial and technological applications.[30,31] Recently, *ab initio* method has been employed to find the elastic anisotropy, hardness, thermal conductivity anisotropy and electronic structure of Ti_4AlC_3, Zr_4AlC_3, and Hf_4AlC_3. Moreover, a comparative analysis was conducted to understand their potential characteristics. These three compounds have not been synthesized experimentally but their structural and chemical features are studied in details *via* theoretic modeling. The hardness of Zr_4AlC_3 is found lower than Ti_4AlC_3. The thermal conductivity decreases from Ti_4AlC_3 to Zr_4AlC_3 at high temperature. Same trend is also followed by the Debye temperature.[34] In recent years, the study of solid materials under high-pressure conditions has gained significant attention. Researchers are increasingly exploring how extreme pressure influences the configurational, bulk, electronic, and thermal features of various materials. Studies[21–24] have investigated the impact of pressure on the structural, elastic, optical, electrical, and thermodynamic properties of M_2AX phases (M = Ti, V, Nb, Ta, A = In, Sn, Ge, Ga, and Tl). Li

and Wang studied the structural, electronic, and mechanical properties of nanolaminate phase Ti_4GeC_3 with pressure.[35] Recently, pressure effect on different properties of 312 type MAX phases, Zr_3InC_2 and Hf_3InC_2 have been studied which ensured their application as TBC material.[36] However, the research about pressure effect on different properties is limited on 413 MAX phases. Among them, the impact of pressure on the physical properties of Nb_4AlC_3 has been studied recently.[37] This research has explored how external pressure influences structural stability, mechanical behavior, electronic properties, and thermodynamic characteristics. MAX phases are considered as highly promising structural materials for industries operating in extreme environments. Also changing physical properties under pressure is related to industrial applications. Many previous studies[22,23,37] show that MAX phase materials transit from brittle to more ductile behavior under pressure. This is important because enhanced ductility improves their suitability for structural components in critical environments. As a result, studying their mechanical behavior under pressure conditions and assessing their structural stability is significant. This scientific understanding helps enhancing their practical application in demanding fields such as aerospace, nuclear energy, and high-temperature engineering. These studies have played a significant role in inspiring the investigation of pressure effects on the physical properties of M_4AlC_3 (M = Ti, Zr). As far as we know, no research has yet been conducted on how the physical properties of M_4AlC_3 (M = Ti, Zr) compounds are affected by changes in pressure. Therefore, studying the various characteristics under pressure of M_4AlC_3 (M = Ti, Zr) is essential. Understanding how the physical features of the selected compounds behave under pressure, will provide critical insights into their potential applications in high-performance environments. This research investigate the dynamical and thermal stability, changes in structural features, mechanical steadiness and changes in bulk properties as well as optical and thermal characteristics of the M_4AlC_3 (M = Ti, Zr) compound under high-pressure conditions, reaching up to 70 GPa. The goal of the existing work is to search and characterize the behavior of M_4AlC_3 (M = Ti, Zr) under such pressures so that this investigation can contribute to a deeper understanding of their performance in extreme environments.

2. Computational details

To analyze various properties of the studied compounds, calculations were conducted using the plane-wave pseudopotential approach within the Generalized Gradient Approximation (GGA) framework developed by Perdew, Burke, and Ernzerhof (PBE),[38] based on Density Functional Theory (DFT).[39] All simulations were performed using the CASTEP code.[40] Ultrasoft pseudopotentials were applied to describe interactions between ionic cores and valence electrons,[41] considering the valence configurations of Ti ($3p^6\ 3d^2\ 4s^2$), Zr ($5s^2\ 4p^6\ 4d^2$), Al ($3s^2\ 3p^1$), and C ($2s^2\ 2p^2$) in the pseudopotential setup. For Brillouin zone sampling and convergence accuracy, a plane-wave cut-off energy of 400 eV with a $19 \times 19 \times 2$ k-point mesh was used for Ti_4AlC_3, and 420 eV with an $18 \times 18 \times 2$ mesh for

Zr$_4$AlC$_3$. Structural optimizations were carried out using the Broyden–Fletcher–Goldfarb–Shanno (BFGS) minimization method, employing convergence thresholds of 5×10^{-6} eV per atom for energy, 0.01 eV Å^{-1} for maximum force, 0.02 GPa for stress, and 5×10^{-4} Å for maximum displacement.[42] Elastic constants (C_{ij}) were computed using the stress–strain method, while polycrystalline elastic moduli were evaluated using the Voigt–Reuss–Hill approximation.[43] The convergence parameters for these calculations were set to an energy tolerance of 4×10^{-6} eV, force tolerance of 0.01 eV Å^{-1}, and displacement tolerance of 4×10^{-4} Å.[44] Additionally, Mulliken bond populations, electronic density of states (DOS), and optical properties were derived directly from the CASTEP output. Debye temperatures were estimated based on the calculated elastic constants. Phonon dispersion and phonon density of states were determined using Density Functional Perturbation Theory (DFPT) combined with the finite displacement method, as implemented in CASTEP.

Table 1 Wyckoff positions of Ti, Al, C in Ti$_4$AlC$_3$ and Zr, Al, C in Zr$_4$AlC$_3$

System	Compounds	Element	Wyckoff	x	y	z	Ref.
				Atomic positions			
Hexagonal	Ti$_4$AlC$_3$	Ti	4f	0.33	0.667	0.055	34
			4e	0	0	0.16	
		Al	2c	0.33	0.667	0.25	
		C	2a	0	0	0	
			4f	0.667	0.33	0.11	
	Zr$_4$AlC$_3$	Zr	4f	0.33	0.667	0.055	
			4e	0	0	0.16	
		Al	2c	0.33	0.667	0.25	
		C	2a	0	0	0	
			4f	0.667	0.33	0.11	

3. Results and discussion

3.1 Structural properties

Both Ti$_4$AlC$_3$ and Zr$_4$AlC$_3$ crystallize in a hexagonal structure, one of the seven Bravais lattice types. They are categorized under the space group $P6_3/mmc$ (No. 194), which features a primitive lattice along with mirror and glide symmetry planes.[34] The specific Wyckoff positions for each element are provided in Table 1, with Ti/Zr and C atoms occupying two distinct lattice sites. The unit cell of both compounds contain 16 atoms having formula unit, $Z = \dfrac{4f + 4e + 2c + 2a + 4f}{4 + 1 + 3} = \dfrac{16}{8} = 2$, where 8 atoms are present per primitive cell of M$_4$AlC$_3$ (M = Ti, Zr). The optimized structures of both Ti$_4$AlC$_3$ and Zr$_4$AlC$_3$ compound are drawn by using lattice parameters. Fig. 1(a) and (b) show the conventional structures of Ti$_4$AlC$_3$ and Zr$_4$AlC$_3$ respectively.

The lattice constants, unit cell volume, and normalized volume under different pressures are presented in Table 2. The calculated lattice parameters for Ti$_4$AlC$_3$ and Zr$_4$AlC$_3$ closely matched with the experimental values at zero pressure, with only minor deviations attributed to differences in computational methods. A slight overestimation by the GGA–PBE approach is noted, which is a known characteristic of this method and supports the reliability of the current results. Fig. 2 (a–d) illustrates how the lattice parameters 'a' and 'c', the c/a ratio, and the normalized volume change with increasing pressure. Here we observed that as pressure increased, both lattice constants and cell volume are decreased. This is due to enhanced interactions among Ti, Al, and C atoms in Ti$_4$AlC$_3$ and among Zr, Al, and C atoms in Zr$_4$AlC$_3$, leading to stronger bonding, shorter bond lengths, and thus a contraction of the lattice structure. As shown in Table 2, the lattice parameter 'c'
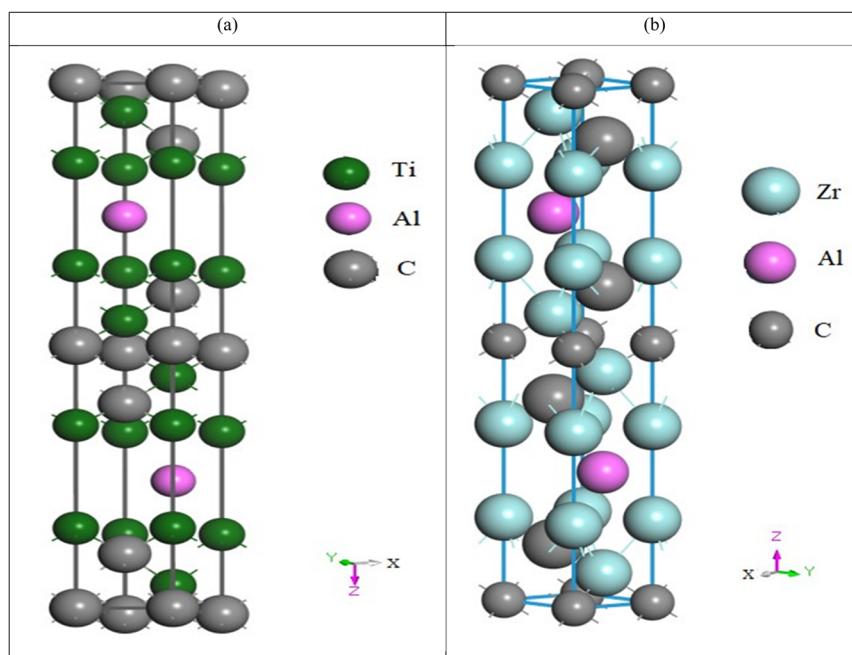

Fig. 1 Conventional crystal structures of (a) Ti$_4$AlC$_3$ and (b) Zr$_4$AlC$_3$ compounds.

Table 2 Lattice constants a (Å), c (Å), volume V (Å^3), normalized volume V/V_0 and formation energy ΔE_f (eV per atom) at high pressure

Phases	Pressure (GPa)	a (Å)	c (Å)	c/a	V (Å^3)	V/V_0	Formation energy, ΔE_f (eV per atom)	Ref.
Ti$_4$AlC$_3$	0	3.060	23.45	7.66	198.80	1.00	−8.68	This study
		3.038	23.234	7.66	—	—	—	34
	10	3.01	22.98	7.63	180.45	0.91	−8.67	This study
	20	2.97	22.62	7.62	173.08	0.87	−8.68	
	30	2.93	22.32	7.61	167.04	0.84	−8.57	
	40	2.91	22.08	7.59	161.88	0.81	−8.50	
	50	2.88	21.87	7.59	157.45	0.79	−8.42	
	60	2.86	21.67	7.57	153.41	0.77	−8.33	
	70	2.84	21.48	7.56	149.77	0.75	−8.24	
Zr$_4$AlC$_3$	0	3.310	25.18	7.60	239.69	1.00	−8.92	This study
		3.298	24.972	7.57	—	—	—	34
	10	3.26	24.65	7.56	226.94	0.95	−8.90	This study
	20	3.21	24.23	7.55	216.89	0.90	−8.84	
	30	3.18	23.87	7.51	209.01	0.87	−8.76	
	40	3.15	23.55	7.48	201.74	0.84	−8.67	
	50	3.12	23.22	7.44	195.26	0.81	−8.55	
	60	3.09	22.94	7.42	189.57	0.79	−8.43	
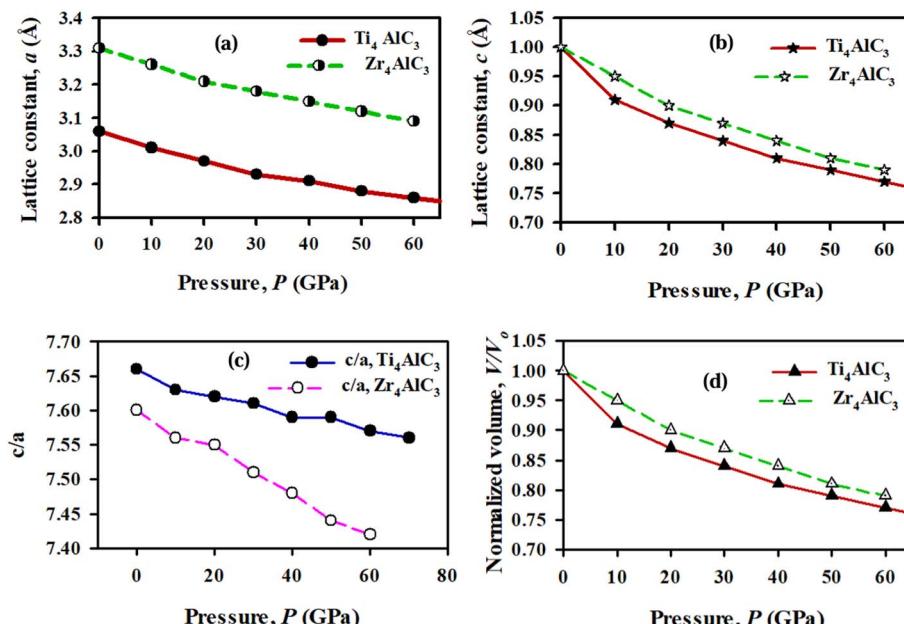
Fig. 2 Structural parameters of the Ti$_4$AlC$_3$ and Zr$_4$AlC$_3$; (a) lattice constant a (Å) (b) lattice constant c (Å) and (c) c/a ratio under pressure (d) normalized cell volume ratio (V/V_0) under pressure.

decreases more rapidly than 'a', indicating that the materials undergo greater compression along the c-axis than along the a-axis.

Determining the formation energy is essential for assessing the crystal stability of a solid. To evaluate the pressure-dependent stability of the investigated compounds, the formation energy was calculated using the following equation:

$$\Delta E_f = \frac{E_{\text{total}}(\text{M}_4\text{AlC}_3) - E_s(\text{M}) - E_s(\text{Al}) - E_s(\text{C})}{N}$$

where, M = Ti, Zr.

Here, $E_s(\text{M})$, $E_s(\text{Al})$, $E_s(\text{C})$ and E_{total} (M$_4$AlC$_3$) represent the energy of M, (M = Ti, Zr), Al, C and M$_4$AlC$_3$, where (M = Ti, Zr)

and N denotes the number of atoms in the unit cell. For being thermodynamically stable, the titled phases need a negative formation energy.[45] The calculated negative values of the formation energy (Table 2) for both compounds throughout all the pressure confirms the chemical and thermodynamic stability.

Every materials have chance to going dynamically unstable as they are normally experienced time-relevant mechanical stress.[46] Since the check in dynamical stability is very imperative for device applications. The dynamical stability of materials is understand by phonon dispersion curve (PDC) analysis where the absence of imaginary frequency ensures the dynamically
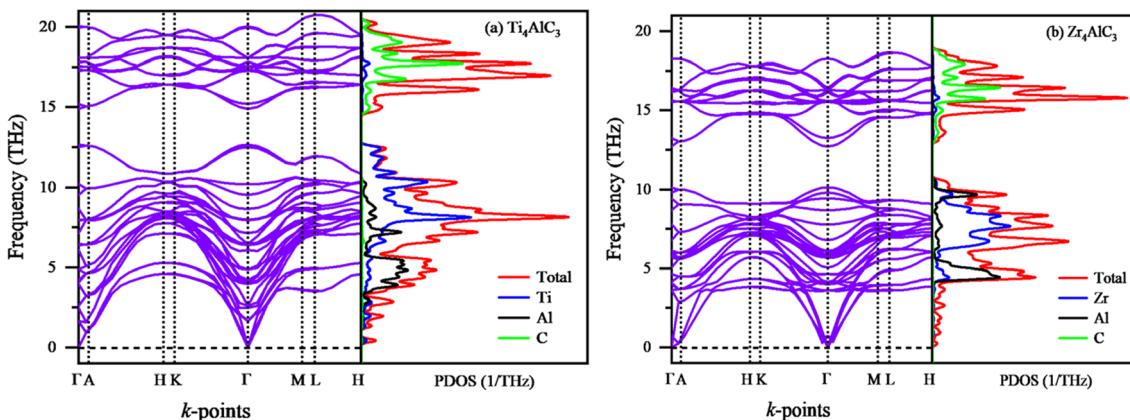
Fig. 3 Phonon dispersion curves of (a) Ti_4AlC_3 and (b) Zr_4AlC_3.

stable nature and the presence of imaginary frequency inform the dynamical instability of material. Fig. 3(a and b) indicate the phonon dispersion curves with phonon density of states of M_4AlC_3 (M = Ti, Zr) along the high symmetry direction Γ–A–H–K–Γ–M–L–H. After analyzing the Fig. 3(a and b) we have noticed that the vibrational frequencies of these materials are positive confirming the dynamical stable nature of M_4AlC_3 (M = Ti, Zr).

Since the unit cell of M_4AlC_3 (M = Ti, Zr) contains 16 atoms (8 atoms per primitive cell) therefore there exist 48 modes according to $3n$ formula. Among 48 modes there're 45 optical modes and 3 acoustic modes whereas the upper energy's optical modes are created by lighter atoms (C, Si) and lower energy's optical modes and acoustic modes are created by heavier atoms (Ti, Zr) with little bit contribution of lighter atoms (C, Si). The dispersive manner of low energies' optical phonon modes have been observed which are overlapped with the acoustic branches. The phononic band gap between the lower optical modes and high frequency's optical modes is observed in materials Ti_4AlC_3 and Zr_4AlC_3 which is mainly raised from mass difference. Here three different regions are perceived in the phonon dispersion curves recommended the phononic characteristics of Ti_4AlC_3 and (b) Zr_4AlC_3 materials.

3.2 Mechanical constancy and bulk features

Elastic properties describe a material's ability to return to its original shape after deformation. Analyzing these properties helps determine a material's suitability for engineering, construction, and manufacturing, ensuring better performance, durability, and reliability. The elastic rigidity coefficients are very important parameters as they associated with brittleness, ductility, mechanical stability and stiffness of materials.[47,48] These properties provide valuable information about how

atoms within a substance are bonded, how they respond to external forces and how the material maintains its stability under various conditions.[49] Hence, in order to understand the mechanical properties of M_4AlC_3 (M = Ti, Zr) and response of these materials under pressure, it is very important to investigate the elastic constants.

The mechanical response of the MAX-phase compounds M_4AlC_3 (M = Ti, Zr) has been analyzed using the strain–stress methodology.[50] This method is incorporated within the CASTEP computational framework. The elastic constants can be determined using the mathematical relationship:

$$\sigma_{ij} = \sum_{ij} C_{ij}\delta_{ij} \tag{1}$$

where σ_{ij} represents the stress tensor corresponding to a specific set of applied strains δ_{ij}. Since both Ti_4AlC_3 and Zr_4AlC_3 belongs to hexagonal structure, they possess only five independent elastic constants: C_{11}, C_{12}, C_{13}, C_{33} and C_{44}. Additionally, it has one dependent elastic constant C_{66}, defined by the relation $C_{66} = (C_{11} - C_{12})/2$. Before further analysis, it is essential to verify the mechanical stability of both hexagonal compounds Ti_4AlC_3 and Zr_4AlC_3. This can be done by applying the well-established stability criteria formulated by Born[51] which is grounded on the stiffness constants (C_{ij}):

$$\left.\begin{array}{c} C_{11} > 0, C_{33} > 0, C_{44} > 0, C_{11} - C_{12} > 0 \\ (C_{11} + C_{12})C_{33} - 2C_{13}^{2} > 0 \end{array}\right\} \tag{2}$$

However, to demonstrate mechanical stability under pressure, a hexagonal crystal system must meet the following conditions:[24]

$$\widetilde{C_{11}} > 0, \widetilde{C_{33}} > 0, \widetilde{C_{44}} > 0, \widetilde{C_{11}} - \widetilde{C_{12}} > 0, \left(\widetilde{C_{11}} + \widetilde{C_{12}}\right)\widetilde{C_{33}} - 2\widetilde{C_{33}}^{2} > 0; \text{ where } \widetilde{C_{\alpha\alpha}} = C_{\alpha\alpha} - P, \alpha\alpha = 11, 33, 44; \widetilde{C_{12}} = C_{12} + P, \widetilde{C_{13}}$$
$$= C_{13} + P. \tag{3}$$

Table 3 Elastic stiffness constants, C_{ij} (in GPa) of M_4AlC_3 (M = Ti, Zr) compounds with the variation of pressure

Phases	Pressure (GPa)	C_{11}	C_{12}	C_{13}	C_{33}	C_{44}	C_{66}	$C_{P (001)} = C_{12} - C_{66}$	$C_{P (100)} = C_{13} - C_{44}$	Ref.
Ti_4AlC_3	0	400.47	84.69	80.74	339.81	142.39	157.89	−73.20	−61.65	This study
Hf_4AlC_3	0	400.30	76.30	70.40	312.0	155.4	—	—	—	34
Nb_4AlC_3	0	411.80	91.70	96.90	330.8	158.1	155.12	—	—	37
Ti_4AlC_3	10	427.05	116.81	128.60	354.03	169.15	177.18	−63.61	−55.15	This study
	20	467.93	113.57	122.03	413.14	187.32	188.54	−50.76	−45.09	
	30	514.86	137.78	149.73	452.76	194.82	198.34	−31.71	−29.23	
	40	563.30	166.63	186.74	511.67	215.97	212.62	−23.55	−20.86	
	50	614.30	189.07	215.04	547.96	235.90	216.57	1.86	−1.29	
	60	651.57	218.43	244.23	589.75	245.52	221.84	27.94	21.07	
	70	693.46	249.78	277.69	628.89	256.62	232.74	41.83	26.91	
		740.05	274.57	305.57	634.0	278.66				
Zr_4AlC_3	0	348.19	79.26	79.90	283.31	113.89	134.47	−52.21	−33.99	This study
Hf_4AlC_3	0	355.30	75.40	78.90	287.60	133.00	—	—	—	34
Nb_4AlC_3	0	411.80	91.70	96.90	330.8	158.1	155.12	—	—	37
Zr_4AlC_3	10	427.05	116.81	128.60	354.03	169.15	146.98	−38.66	−24.27	This study
	20	402.28	108.32	115.39	341.58	139.66	159.51	−23.74	−13.68	
	30	454.78	135.77	153.08	393.52	166.76	164.71	−0.01	3.28	
	40	494.11	164.70	183.89	420.93	180.61	166.00	20.44	17.29	
	50	518.44	186.44	212.64	419.36	195.35	163.58	52.02	35.73	
	60	542.76	215.60	242.99	433.62	207.26	155.95	90.24	59.56	
		558.18	246.19	267.34	483.81	207.78				

The elastic constants of M_4AlC_3 (M = Ti, Zr) are calculated up to 70 GPa and 60 GPa for Ti_4AlC_3 and Zr_4AlC_3 have been listed in Table 3 with previous calculated data available in literature.[34] The calculated elastic constants show good agreement with the previous study at zero pressure. A slight discrepancy is observed in elastic parameters between the present calculated and previous theoretical values at zero pressure. This deviation occurred due to the usage of different methodology. For ensuring the accuracy of our investigated result, we have listed some similar types of MAX compounds (Nb_4AlC_3, Hf_4AlC_3) for comparison. Almost analogous values have been observed of the studied phases M_4AlC_3 (M = Ti, Zr) compared to other similar types of compounds. Both the compounds Ti_4AlC_3 and Zr_4AlC_3 satisfied all the necessary conditions for mechanical stability under pressure ensures the mechanical stability of the titled phases. However, this stability is based solely on theoretical analysis as there is no experimental data available in literature regarding the material's mechanical properties under pressure.

The variation of elastic constants C_{ij} of M_4AlC_3 (M = Ti, Zr) are shown in Fig. 4(a and b). As shown in Fig. 4(a and b), the elastic constants of M_4AlC_3 (M = Ti, Zr) show increased manner with pressure. For pressure up to 60 GPa (for Ti_4AlC_3) and up to 30 GPa (for Zr_4AlC_3) the variations in the values of C_{ij} follow a linear trend, maintaining the relationship described by Hooke's law, (where stress is proportional to strain). This linear increase suggests a typical elastic response under pressure. However, after 60 GPa (for Ti_4AlC_3) and 30 GPa (for Zr_4AlC_3) a slight deviation from the linear response is observed which indicate the system is no longer follows Hooke's law. This could be indicative of a phase transition occurring at around 60 GPa and 30 GPa in Ti_4AlC_3 and Zr_4AlC_3 respectively. The higher limit of pressure was selected based on the observed pressure induced phase transition. Ti_4AlC_3 exhibit phase transition near 60 GPa, so properties calculation was extended up to 70 GPa. On the other hand, Zr_4AlC_3 shows phase transition after 30 GPa, so calculations were extended up to 60 GPa. This helps to study the behavior after phase transition. Since the transition pressure was different for different compounds, the higher limit was chosen accordingly.

The elastic constant C_{11} indicates the material's resistance to uniaxial compression or tension along the a-axis ([52] direction), while C_{33} represents resistance along the c-axis ([001] direction).[53–55] As shown in Fig. 4(a and b), both compounds

exhibit an increase in these stiffness constants with rising pressure. A higher C_{11} implies stronger resistance to deformation along the a-axis, while an increasing C_{33} indicates enhanced resistance along the c-axis, suggesting stronger interlayer bonding.[55,56] Throughout the pressure range of 0–70 GPa, C_{11} remains consistently greater than C_{33}, implying that more pressure is needed to induce plastic deformation along the a-axis than the c-axis. This trend aligns with typical MAX phase behavior, where in-plane bonding is stronger than interlayer interactions.[21,55]

C_{12} and C_{13} are referred to as the in-plane and cross-plane coupling moduli, respectively. They describe the material's response to shear stress along the a-axis when uniaxial strain is applied along the b- and c-axes. As shown in Fig. 4(a and b), both C_{12} and C_{13} increase with applied pressure, indicating that the materials become more resistant to shear deformation in the b- and c-directions under stress along the a-axis.[56] C_{44} measures the resistance to shear deformation within the basal plane and is closely associated with material hardness.[57] The calculated values of C_{44} of both the materials M_4AlC_3 (M = Ti, Zr) are greater than 100 GPa confirming high strength against shear deformation. Here the phase Ti_4AlC_3 exhibits higher C_{44} therefore it is harder than the other phase Zr_4AlC_3.

These elastic stiffness constants are essential for calculating polycrystalline mechanical properties such as bulk modulus (B), shear modulus (G), Young's modulus (E), Poisson's ratio (ν), and Pugh's ratio (B/G). Understanding how these properties vary with pressure is vital for assessing mechanical performance. The bulk and shear moduli are commonly derived using the Voigt (V),[50] Reuss (R),[58] and Voigt–Reuss–Hill (VRH)[59] averaging methods, based on the following equations:

$$B_V = \frac{[2(C_{11} + C_{12}) + C_{33} + 4C_{13}]}{9} \quad (4)$$

$$B_R = \frac{(C_{11} + C_{12})C_{33} - 2C_{13}{}^2}{C_{11} + C_{12} + 2C_{33} - 4C_{13}} \quad (5)$$

$$G_V = \frac{1}{30}(C_{11} + C_{12} + 2C_{33} - 4C_{13} + 12C_{44} + 12C_{66}) \quad (6)$$

$$G_R = \frac{\frac{5}{2}\left[(C_{11} + C_{12})C_{33} - 2C_{13}{}^2\right]C_{44}C_{66}}{\left[3B_V C_{44}C_{66} + ((C_{11} + C_{12})C_{33} - 2C_{13}{}^2)(C_{44} + C_{66})\right]} \quad (7)$$
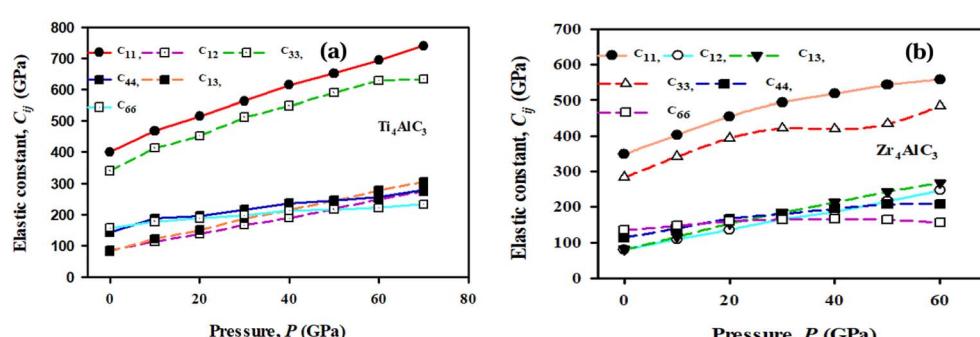

Fig. 4 Elastic stiffness parameters of (a) Ti_4AlC_3 and (b) Zr_4AlC_3 under pressure.

Table 4 Computed values of bulk modulus (B, in GPa), shear modulus (G, in GPa), Young's modulus (E, in GPa), Pugh's ratio (B/G), machinability index ($\mu_m = B/C_{44}$), Poisson's ratio (ν), and hardness (H_v, in GPa) for M_4AlC_3 (M = Ti, Zr) compounds under different pressure conditions

Phase	Pressure	B	G	E	B/G	μ_m	ν	H_v	Ref.
Ti_4AlC_3	0	180.90	147.87	348.81	1.22	1.27	0.18	25.15	This study
		170.60	153.70	354.60	1.11	—	0.15	—	34
Hf_4AlC_3	0	190.90	152.50	361.40	1.25	—	0.19	—	
Nb_4AlC_3	0	216.78	153.15	371.87	1.42	1.28	0.21	29.71	37
Ti_4AlC_3	10	229.10	175.93	420.24	1.30	1.22	0.19	26.49	This study
	20	261.81	184.77	426.91	1.41	1.34	0.21	24.94	
	30	301.94	198.40	488.26	1.52	1.39	0.23	24.16	
	40	334.81	212.67	526.52	1.57	1.42	0.25	24.42	
	50	367.27	219.09	548.25	1.67	1.50	0.26	22.42	
	60	402.77	225.89	570.93	1.78	1.57	0.27	22.12	
	70	431.14	236.53	599.89	1.82	1.55	0.27	22.29	
Zr_4AlC_3	0	161.29	121.29	290.94	1.33	1.42	0.20	19.88	This study
		162.10	131.70	311.00	1.23	—	0.18	—	34
Hf_4AlC_3	0	190.90	152.50	361.40	1.25	—	0.19	—	
Nb_4AlC_3	0	216.78	153.15	371.87	1.42	1.28	0.21	29.71	37
Zr_4AlC_3	10	202.27	138.67	338.63	1.46	1.45	0.22	19.68	This study
	20	242.71	155.19	383.78	1.56	1.46	0.24	19.67	
	30	274.47	162.25	406.62	1.69	1.52	0.25	18.58	
	40	296.89	164.48	416.53	1.81	1.52	0.27	17.43	
	50	323.57	165.39	423.95	1.96	1.56	0.28	15.96	
	60	350.87	165.09	428.12	2.13	1.69	0.30	14.51	

$$B = \tfrac{1}{2}(B_V + B_R) \quad (8)$$

$$G = \tfrac{1}{2}(G_V + G_R) \quad (9)$$

In this context, B_V and G_V represent the bulk and shear moduli from the Voigt model, while B_R and G_R are derived from the Reuss model. The averaged values of bulk (B) and shear (G) moduli are then used to compute Young's modulus (E) and Poisson's ratio (ν) using standard formulas:[51]

$$E = \frac{9BG}{3B + G} \quad (10)$$

$$\nu = \frac{3B - 2G}{2(3B + G)} \quad (11)$$

The machinability index can be obtained by following equation:[60]

$$\mu_m = \frac{B}{C_{44}} \quad (12)$$

The hardness of both materials is pressure-dependent and estimated using standard formulas.[61,62]

$$H_V = \frac{(1 - 2\nu)E}{6(1 + \nu)} \quad (13)$$

Table 4 presents the calculated values of B, G, E, B/G, μ_m, ν, and H_v under varying pressures. The zero-pressure results align well with previous studies, supporting the accuracy of the present calculations. As shown in Table 4 and Fig. 5(a and b), the values of bulk (B), shear (G), and Young's (E) moduli are increased with increasing pressure, indicating enhanced bonding strength. On the basis of Bulk, shear and Young's modulus at zero pressure, the studied and referenced compounds can be arranged as $Nb_4AlC_3 > Hf_4AlC_3 > Ti_4AlC_3 >$
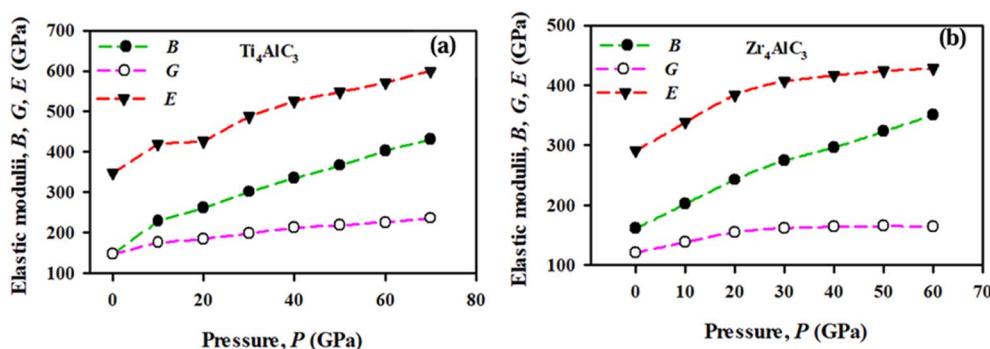

Fig. 5 Elastic moduli B, G and E of (a) Ti_4AlC_3 and (b) Zr_4AlC_3 under pressure.
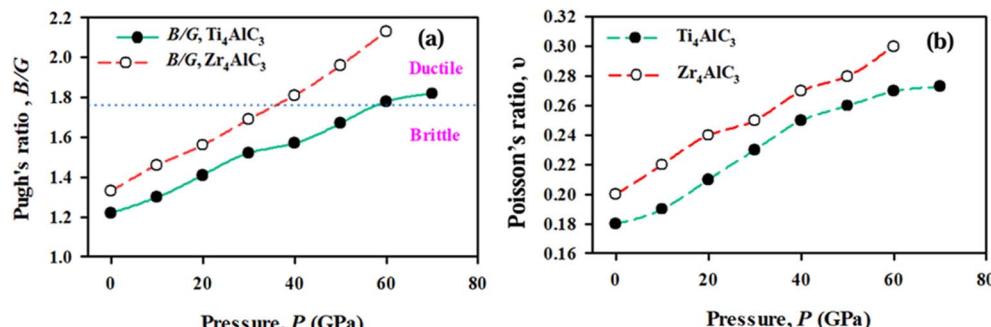
Fig. 6 (a) Pugh's ratio (B/G) and (b) Poisson's ratio (ν) of M_4AlC_3 (M = Ti, Zr) compounds at different pressure.

Zr_4AlC_3. Here, among all the materials Nb_4AlC_3 has highest bulk, shear and Young's moduli indicating its strongest resistance towards volume deformation, shear deformation and more stiffness respectively.

To measure the resistance of solids to volume changes, the bulk moduli, B is a good indicator can be used to predict the fracture and compressing resistance of solids.[63] The shear modulus, G is used to measure the resistance of solids to shape changes and measure the plastic deformation depending on the value of C_{44}.[64] On the other hand, the Young's modulus, E explains the ratio of stress and strain, and measures the rigidity of solids. The superior Young's modulus indicates the more solid's ability to deform.[65] Fig. 5 (a and b) indicates that the values of B, G, and E are increased with pressure, indicating that the resistance to volume, shape and longitudinal deformation increased linearly with pressure. The value of B exceeded the critical value 100 GPa for both compounds, confirming that they are hard materials. Ti_4AlC_3 consistently shows higher B, G and E values than Zr_4AlC_3, suggesting greater resistance to both volumetric and shear deformation, and improved structural stability under stress.

Young's modulus (E) is a key bulk property that measures a material's stiffness and its resistance to linear deformation under stress. It also correlates with thermal shock resistance (R), as defined by the following equation:[66]

$$R = \frac{\{\sigma_f (1 - \nu)\}}{\{E\alpha\}} \quad (14)$$

In the thermal shock resistance equation, σ_f is the bending strength, ν is Poisson's ratio, and α is the thermal expansion coefficient. Since thermal shock resistance (R) is inversely related to Young's modulus (E), materials with lower E are better suited for thermal barrier coatings (TBCs). Given their high E values, Ti_4AlC_3 and Zr_4AlC_3 are not ideal for TBC applications.

Pugh's ratio (B/G), which compares bulk to shear modulus, indicates ductility-materials with $B/G > 1.75$ are ductile, while lower values suggest brittleness.[64] As shown in Table 4 and Fig. 6(a), both compounds initially exhibit brittle behavior. Ti_4AlC_3 transitions to ductile above 60 GPa, and Zr_4AlC_3 above 40 GPa. This pressure-induced ductility enhances their suitability for industrial applications under high-pressure conditions.

Poisson's ratio (ν) is another indicator of a material's ductility, with 0.26 as the critical threshold—values above indicate ductility, below indicate brittleness.[67] In this study, Ti_4AlC_3 transitions from brittle to ductile at 60 GPa, and Zr_4AlC_3 at 40 GPa, showing improved deformability under pressure. Poisson's ratio also reflects bonding type: metallic bonds typically have $\nu \approx 0.10$, covalent ≈ 0.33.[68] Values between 0.18–0.30 for both compounds suggest mixed metallic-covalent bonding. Moreover, Poisson's ratio can distinguish central force solids ($\nu = 0.25$–0.50) from non-central ones.[69] Ti_4AlC_3 and Zr_4AlC_3 are non-central force solids below 40 GPa and 30 GPa respectively, becoming central force solids beyond those pressures.

Cauchy Pressure (CP), calculated as C_{13}–C_{44} (for the (100) plane) or C_{12}–C_{66} (for the (001) plane), further indicates bonding and ductility.[70] Positive CP suggests metallic and ductile behavior; negative CP indicates covalent and brittle nature.[71] CP becomes positive at 60 GPa for Ti_4AlC_3 and 40 GPa
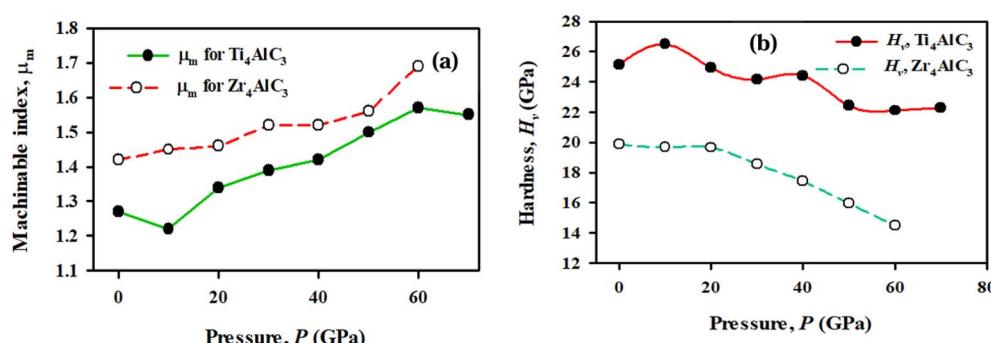

Fig. 7 (a) Machinability index, μ_m and (b) hardness, H_v of M_4AlC_3 (M = Ti, Zr) compounds at different pressure.

for Zr$_4$AlC$_3$, consistent with B/G and ν trends. However, at 50 GPa (Ti$_4$AlC$_3$) and 30 GPa (Zr$_4$AlC$_3$), CP shows mixed values across planes—suggesting a transitional bonding state requiring deeper analysis. The machinability index (MI = B/C_{44}) assesses how easily a material can be machined—higher MI indicates better machinability and lower tool wear. MI increases with pressure for both compounds, with Ti$_4$AlC$_3$ showing better machinability than Zr$_4$AlC$_3$. From Fig. 7(a and b), ductility and machinability improve under pressure.

Hardness (H_v), which measures resistance to plastic deformation, inversely affects machinability. It is an essential macroscopic factor used for technological and industrial applications lower hardness supports easier shaping and cutting whereas a hard material has ability to resist plastic deformation from the irreversible motion of atom. The calculated hardness from zero to high pressure of the studied phases are listed in Table 4. As pressure increases, the hardness of both materials decreases, which aligns with the inverse relationship between Pugh's ratio (B/G) and hardness. A higher B/G indicates greater ductility and lower hardness, improving machinability. Ti$_4$AlC$_3$ has higher hardness than Zr$_4$AlC$_3$ due to stronger atomic bonding from its smaller atomic radius. This is significant for industrial applications, as materials with higher machinability improve production efficiency, reduce tool wear, and lower energy consumption. The consistency between hardness, Pugh's ratio, and machinability index under pressure confirms the reliability of these parameters for high-pressure machining.

3.3 Insights of anisotropy

Material properties vary due to crystal anisotropy, which affects phenomena such as reaction kinetics, phonon behavior, and fracture mechanics. Understanding anisotropy helps explain material responses under different conditions.[72] Table 3 shows that $C_{11} > C_{33}$, confirming anisotropic elasticity, which also impacts polycrystalline moduli.[73] MAX-phase carbides display anisotropy due to their atomic arrangement, leading to directional variations in mechanical properties.[74] To quantify this, we use indices like universal anisotropy (A^U), shear anisotropic

factors (A_1, A_2, A_3), percentage anisotropy (A_B, A_G), and 3D plots of elastic stiffness parameters.[75]

$$A_1 = \frac{C_{11} + C_{12} + 2C_{33} - 4C_{13}}{6C_{44}} \tag{15}$$

$$A_2 = \frac{4C_{44}}{C_{11} + C_{33} - 2C_{13}} \tag{16}$$

$$A_3 = \frac{C_{11} + C_{12} + 2C_{33} - 4C_{13}}{3(C_{11} - C_{12})} \tag{17}$$

A_1, A_2 and A_3 represent shear anisotropy in the {100}, {010}, and {001} planes, linked to specific crystallographic directions. For isotropic crystals, $A_i = 1$ ($i = 1, 2, 3$); deviations indicate anisotropy. As shown in Table 5, both Ti$_4$AlC$_3$ and Zr$_4$AlC$_3$ exhibit elastic anisotropy, with shear anisotropy factors varying with pressure depending on the crystal plane. Both compounds show a similar trend, suggesting a parallel pressure response. To further quantify anisotropy, percentage anisotropy for bulk (A_B) and shear modulus (A_G) is calculated using Ranganathan and Ostoja-Starzewsky's method.[76]

$$A_B = \frac{B_V - B_R}{B_V + B_R} \times 100\% \tag{18}$$

$$A_G = \frac{G_V - G_R}{G_V + G_R} \times 100\% \tag{19}$$

Ranganathan and Ostoja-Starzewsky proposed the universal anisotropy index (A^U) as a standard metric to quantify elastic anisotropy in crystals, calculated using the following equation:[77]

$$A^U = \frac{5G_V}{G_R} + \frac{B_V}{B_R} - 6 \quad \geq 0 \tag{20}$$

B_V, B_R, G_V, and G_R are derived from Voigt and Reuss approximations. Zero values of A_B, A_G, and A^U indicate isotropy, while non-zero values confirm anisotropy. As shown in Table 5, both Ti$_4$AlC$_3$ and Zr$_4$AlC$_3$ exhibit anisotropic behavior under pressure. Positive A_B and A_G, reflect directional dependence of bulk and shear moduli, with shear anisotropy showing a stronger

Table 5 Various anisotropy indices—shear factors (A_1, A_2, A_3), percentage anisotropy (A_B and A_G), universal anisotropy (A^U), Zener's index (A_Z), and compressibility ratio (k_c/k_a) for Ti$_4$AlC$_3$ and Zr$_4$AlC$_3$

Elements	Pressure	A_1	A_2	A_3	A_B	A_G	A^U	A_Z	k_c/k_a	Ref.
Ti$_4$AlC$_3$	0	0.985	0.984	0.889	0.304	0.21	0.02	0.902	1.25	This study
	10	0.818	1.176	0.865	0.113	0.30	0.03	1.057	1.16	
	20	0.821	1.170	0.848	0.080	0.12	0.03	1.033	1.17	
	30	0.777	1.230	0.846	0.030	0.43	0.04	1.240	1.10	
	40	0.734	1.289	0.815	0.135	0.15	0.06	1.109	1.12	
	50	0.728	1.304	0.825	0.040	0.68	0.07	1.134	1.10	
	60	0.708	1.338	0.819	0.030	0.81	0.08	1.157	1.10	
	70	0.634	1.460	0.759	0.140	1.42	0.15	1.197	1.23	
Zr$_4$AlC$_3$	0	0.987	0.966	0.836	0.420	0.44	0.05	0.847	1.32	
	10	0.874	1.089	0.830	0.220	0.28	0.03	0.950	1.24	
	20	0.765	1.230	0.800	0.100	0.24	0.03	1.045	1.18	
	30	0.706	1.320	0.774	0.005	0.69	0.07	1.097	1.23	
	40	0.591	1.525	0.696	0.290	1.92	0.20	1.177	1.35	
	50	0.526	1.691	0.666	0.350	2.86	0.30	1.267	1.43	
	60	0.564	1.640	0.750	0.130	2.33	0.24	1.332	1.25	

pressure response. Additionally, the increasing A^U with pressure indicates growing elastic anisotropy due to unequal changes in bulk and shear moduli across crystallographic directions. The Zener anisotropy factor, A_Z is a crucial parameter in determining the mechanical behavior of a solid as it indicates whether the material exhibits direction-dependent or direction-independent elastic properties. It is calculated by following equation:[78]

$$A_Z = \frac{2C_{44}}{(C_{11} - C_{12})} \quad (21)$$
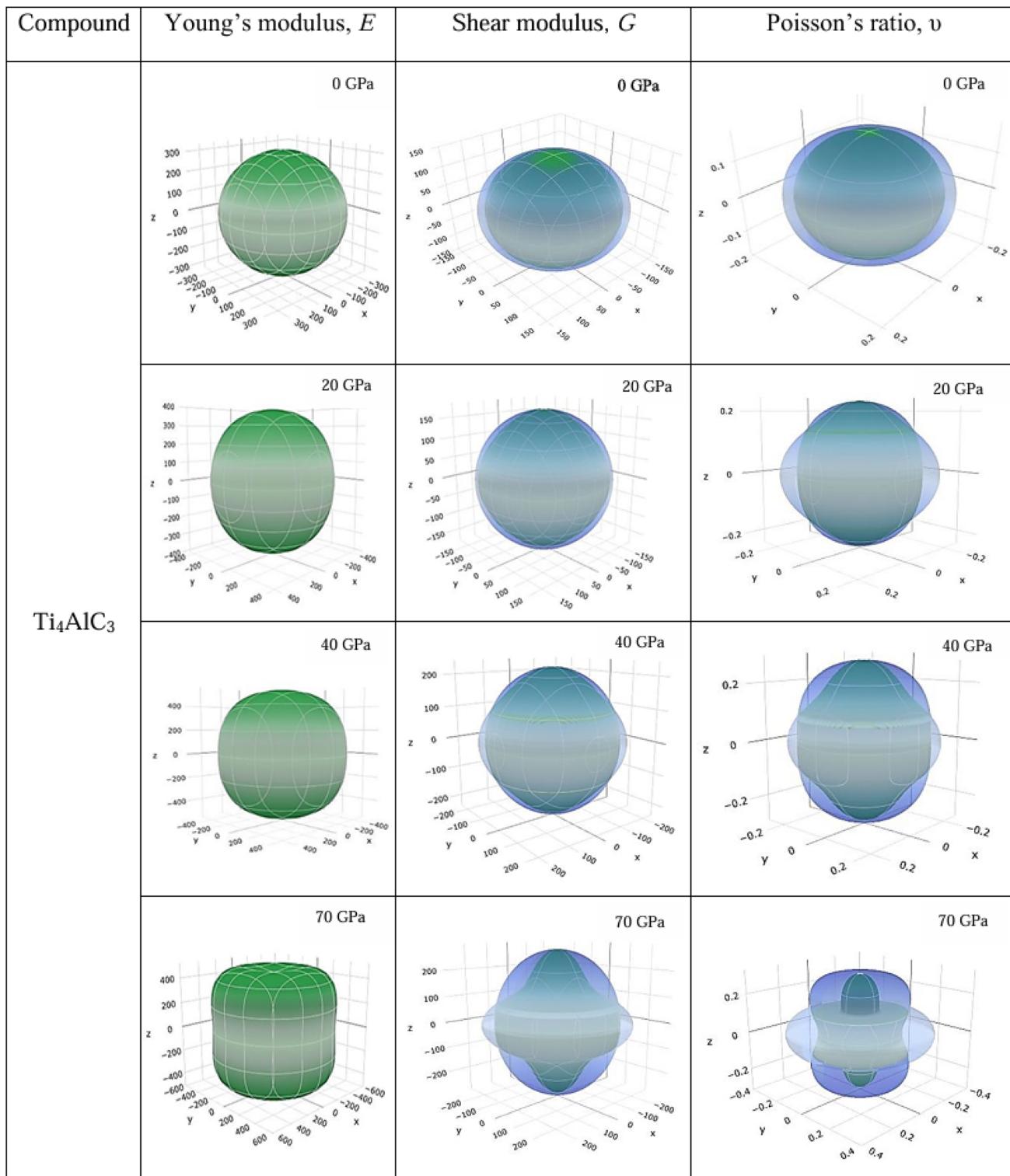
Fig. 8   3D distributions of Young's modulus (E), shear modulus (G), and Poisson's ratio (ν) for Ti_4AlC_3 under varying pressures.

A Zener factor of 1 indicates isotropy, while values differing from 1 reflect anisotropy. As shown in Table 5, the Zener anisotropy factor (A_Z) for both compounds exceeds 1 and rises with pressure, indicating increasing anisotropy under compression. In hexagonal structures, compressibility anisotropy is also described by the ratio k_c/k_a, comparing linear compressibility along the c- and a-axes.[79]
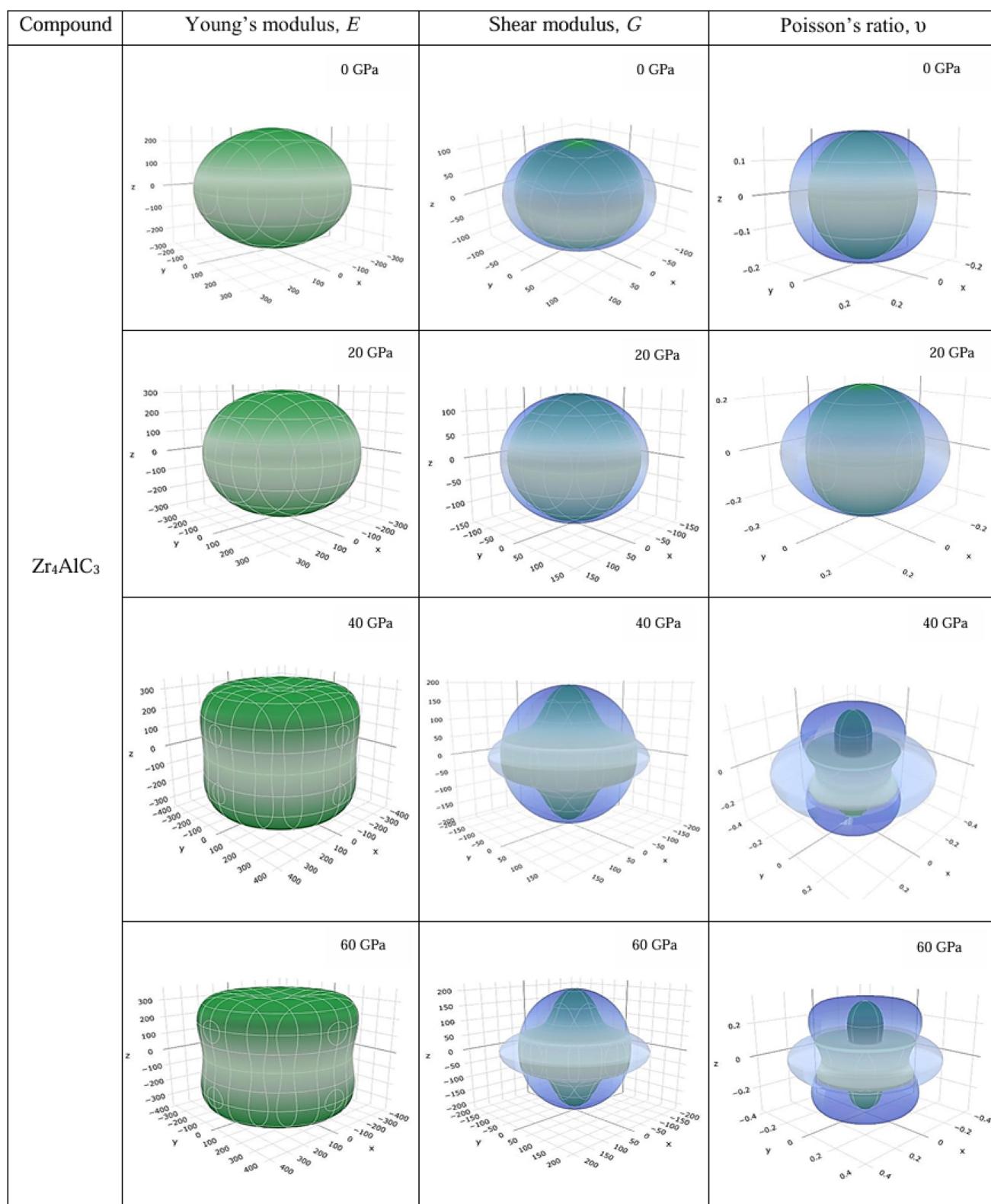
Fig. 9   3D distributions of Young's modulus (E), shear modulus (G), and Poisson's ratio (v) for Zr_4AlC_3 under varying pressures.

$$\frac{K_c}{K_a} = \frac{C_{11} + C_{12} - 2C_{13}}{C_{33} - C_{13}} \qquad (22)$$

A k_c/k_a value of 1 indicates equal compressibility along the c- and a-axes, reflecting isotropy. However, Table 5 shows values consistently above 1 for both compounds under pressure, suggesting greater compressibility along the c-axis and confirming anisotropic behavior.

To visualize the anisotropic behavior of Ti_4AlC_3 and Zr_4AlC_3, 3D plots of Young's modulus, shear modulus, and Poisson's ratio were generated using ELATE,[80,81] highlighting directional mechanical variations. Fig. 8 and 9 depict this under pressure, with corresponding maxima and minima detailed in Table 6. In isotropic materials, elastic properties remain uniform in all directions, resulting in spherical 3D plots of elastic moduli.[82] In contrast, anisotropic materials show deviations from this shape, reflecting directional dependence. As shown in Fig. 8 and 9, increasing pressure distorts the spherical shape, indicating enhanced anisotropy. The green surfaces highlight maximum Young's modulus, while blue regions represent maximum shear and Poisson's ratio, with inner green areas denoting their minimum values. From Table 6, for Ti_4AlC_3, Young's modulus increases from 370.03 GPa (max) and 312.93 GPa (min) at 0 GPa to 653.31 GPa and 449.94 GPa at 70 GPa. Shear modulus shows a similar rise. For Zr_4AlC_3, values increase from 315.77 GPa/253.43 GPa (Young's) and 134.47 GPa/113.88 GPa (shear) at 0 GPa to 479.13 GPa/306.11 GPa and 207.78 GPa/124.63 GPa at 60 GPa. These trends align with the universal anisotropy index, confirming that pressure enhances anisotropy and validating the reliability of the study.

3.4 Chemical bonding and electronic characteristics

The electronic structure reveals key insights into conductivity, bonding, and stability, influenced by valence and conduction electrons. Band structures, showing energy dispersion $E(k)$ across the Brillouin zone, classify materials as metals, semi-metals, or insulators. For M_4AlC_3 (M = Ti, Zr) MAX phases, band structures were calculated under pressure. Fig. 10 and 11 display bands for Ti_4AlC_3 (0–70 GPa) and Zr_4AlC_3 (0–60 GPa), with green lines marking electronic states and the Fermi level at 0 eV. Multiple bands cross the Fermi level at all pressures, confirming metallic behavior without a band gap. Initially, bands near the Fermi level are moderately dispersed but widen with pressure, indicating stronger orbital hybridization and increased metallicity, especially in Zr_4AlC_3. The band structure also shows anisotropic conductivity, with lower dispersion along the c-axis (Γ–A, H–K, M–L) and higher dispersion in basal plane directions (A–H, K–Γ, Γ–M, L–H), reflecting pressure-dependent directional electronic behavior.[83]

This study analyzes the electronic density of states (DOS), including total (TDOS) and partial (PDOS), to understand bonding and hybridization in Ti_4AlC_3 and Zr_4AlC_3.[84,85] Fig. 12 shows TDOS under various pressures, considering outer electron configurations: Ti ($3p^6$ $3d^2$ $4s^2$), Zr ($5s^2$ $4p^6$ $4d^2$), Al ($3s^2$ $3p^1$), and C ($2s^2$ $2p^2$). TDOS is evaluated from −5 to 5 eV at pressures of 0, 30, 50, and 70 GPa for Ti_4AlC_3, and 0, 20, 40, and 60 GPa for Zr_4AlC_3. Both compounds show metallic behavior with TDOS at the Fermi level. For Ti_4AlC_3, TDOS at the Fermi level decreases with pressure: 3.86, 3.60, 3.30, and 3.26 states per eV per unit cell (Fig. 12(a)). For Zr_4AlC_3, TDOS increases: 3.85, 4.40, 5.30, and 5.58 states per eV per unit cell (Fig. 12(b)). PDOS for Ti, Zr, Al, and C (Fig. 13 and 14) further detail atomic contributions from −10 to 10 eV, with the Fermi level (0 eV) marked by black dotted lines.

In Ti_4AlC_3 (Fig. 13), the main TDOS peak in the valence band (−5 to −1.8 eV) arises from Ti-3d and C-2p orbitals, with minor Al-3s involvement, reflecting strong Ti–C hybridization. Near the Fermi level, Ti-3d and Al-3p orbitals dominate, while Ti-4s, Al-3s, and C-2p contribute less. At the Fermi level, Ti-3d is the primary contributor; in the conduction band, Ti-3d remains dominant with minor Al-3p and C-2p inputs. Increasing

Table 6 The anisotropy of Young's modulus (E), shear modulus (G), and Poisson's ratio (ν) for Ti_4AlC_3 and Zr_4AlC_3 under pressure is calculated

| Elements	Pressure	Young's modulus (GPa)			Shear modulus (GPa)			Poisson's ratio		
		E_{min}	E_{max}	A_Y	G_{min}	G_{max}	A_G	ν_{min}	ν_{max}	A_ν
Ti_4AlC_3	0	312.93	370.03	1.182	142.39	157.89	1.109	0.166	0.197	1.183
	10	361.92	435.09	1.202	158.35	187.33	1.183	0.143	0.242	1.690
	20	386.91	436.94	1.129	164.73	181.04	1.099	0.207	0.261	1.266
	30	416.12	511.18	1.228	174.35	215.97	1.239	0.171	0.292	1.711
	40	504.56	553.74	1.097	203.95	225.95	1.108	0.221	0.279	1.258
	50	452.63	582.08	1.286	186.81	245.52	1.314	0.173	0.326	1.889
	60	465.38	610.22	1.311	190.21	256.62	1.349	0.176	0.343	1.947
	70	449.94	653.31	1.452	187.63	278.66	1.485	0.150	0.378	2.531
Zr_4AlC_3	0	253.43	315.77	1.246	113.88	134.47	1.181	0.174	0.233	1.337
	10	289.42	350.63	1.211	127.01	146.98	1.157	0.191	0.273	1.432
	20	315.50	369.45	1.171	133.40	152.36	1.142	0.212	0.299	1.409
	30	384.40	441.30	1.267	140.28	184.48	1.315	0.188	0.336	1.791
	40	291.06	458.32	1.575	124.43	195.35	1.570	0.136	0.410	3.020
	50	277.90	477.54	1.718	118.18	207.26	1.754	0.112	0.451	4.027
	60	306.11	479.13	1.565	124.63	207.78	1.667	0.133	0.405	3.046
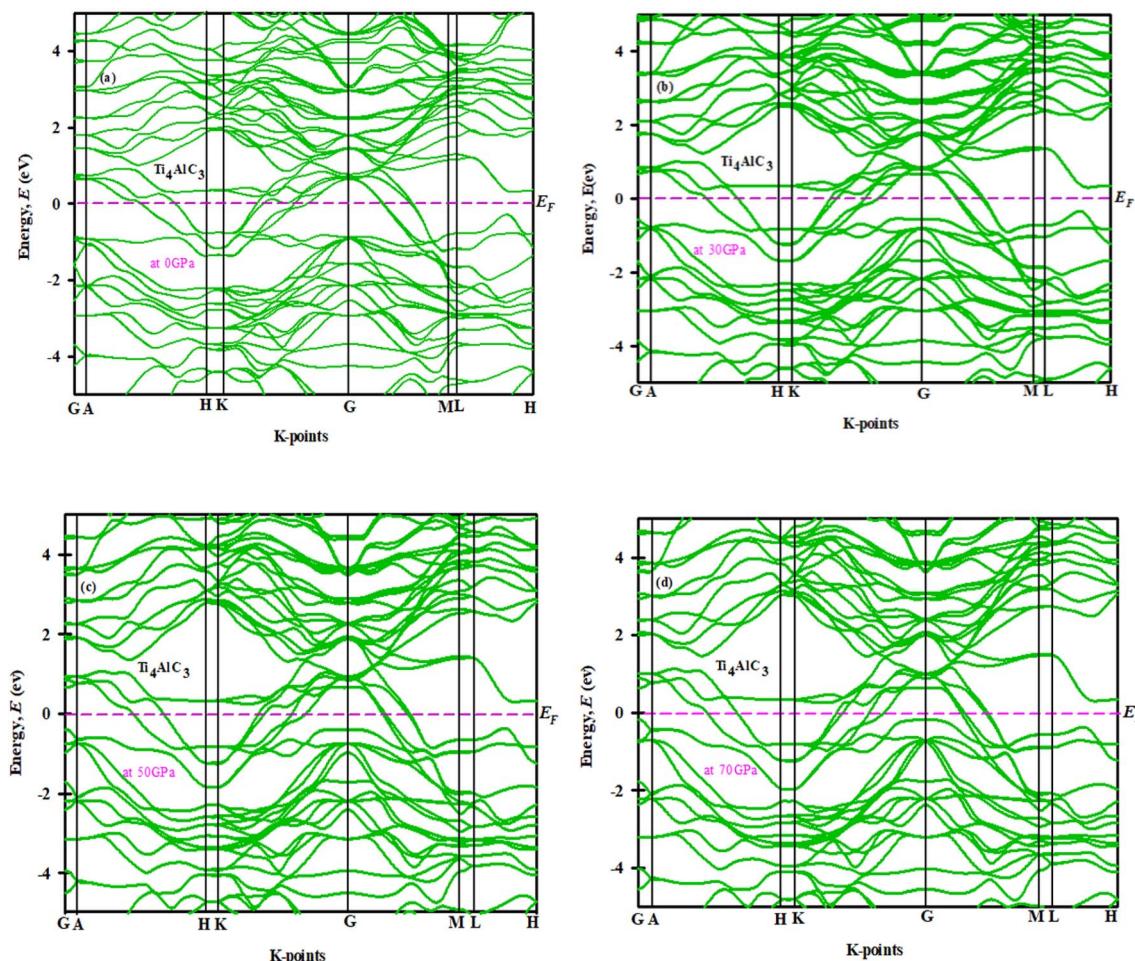
Fig. 10 Electronic band structures of Ti_4AlC_3 at (a) 0, (b) 30, (c) 50, and (d) 70 GPa.

pressure reduces Ti-3d contributions, lowering TDOS. This matches prior MAX phase studies.[86] The stronger Ti–C covalent bond contrasts with the weaker, more metallic Ti–Al bond. For Zr_4AlC_3 (Fig. 14), similar trends appear: Zr-4d dominates valence, Fermi level, and conduction bands; Al-3p gains influence with pressure, increasing TDOS, while C-2p and Zr-4p remain minimal contributors.

The bonding characteristics of M_4AlC_3 (M = Ti, Zr) were analyzed using Mulliken population analysis, which distinguishes between covalent and ionic bonds.[87] Table 7 presents bond lengths, populations, and charges for Ti_4AlC_3 (0–70 GPa) and Zr_4AlC_3 (0–60 GPa). Positive bond populations confirm covalent bonding, while the negative charge on C and Al and positive charge on Ti/Zr indicate charge transfer from metal to non-metal atoms.[88] Ti_4AlC_3 maintains only C–Ti bonds under pressure, showing no structural change. In contrast, Zr_4AlC_3 forms a new Al–Zr bond at 60 GPa, indicating pressure-induced bonding adaptation. Both compounds show decreasing bond population and bond length with pressure, reflecting weaker covalent interactions due to atomic compression.

To investigate atomic charge distribution and bonding in M_4AlC_3 (M = Ti, Zr), charge density maps were generated. Fig. 15 displays these maps for Ti_4AlC_3 at 0 and 70 GPa, and

Zr_4AlC_3 at 0 and 60 GPa, with red indicating high and blue low electron density.

From Fig. 15(a) and (b), at 0 GPa high electron density (red regions) is primarily concentrated around the Ti–C bonds indicating strong covalent interactions. As pressure increases to 70 GPa, the electron density around Ti decreases slightly suggesting a reduction in covalent character and bonding becoming more ionic in nature. From Fig. 15(c) and (d), at 0 GPa high electron density is observed around Zr–C bonds similar to Ti_4AlC_3. However, at 60 GPa a noticeable charge density is observed around Al–Zr which signify the formation of an additional bonding interaction at high pressure. These charge density mappings show good agreement with Table 7 as discussed earlier. The observed trends in charge distribution have consistency with the computed bond population and Mulliken charge values.

3.5 Optical properties

Studying the optical properties of MAX phases M_4AlC_3 (M = Ti, Zr) reveals their electronic structure and interaction with light. Key parameters—photon absorption, reflectivity, dielectric function, refractive index, optical conductivity, and loss
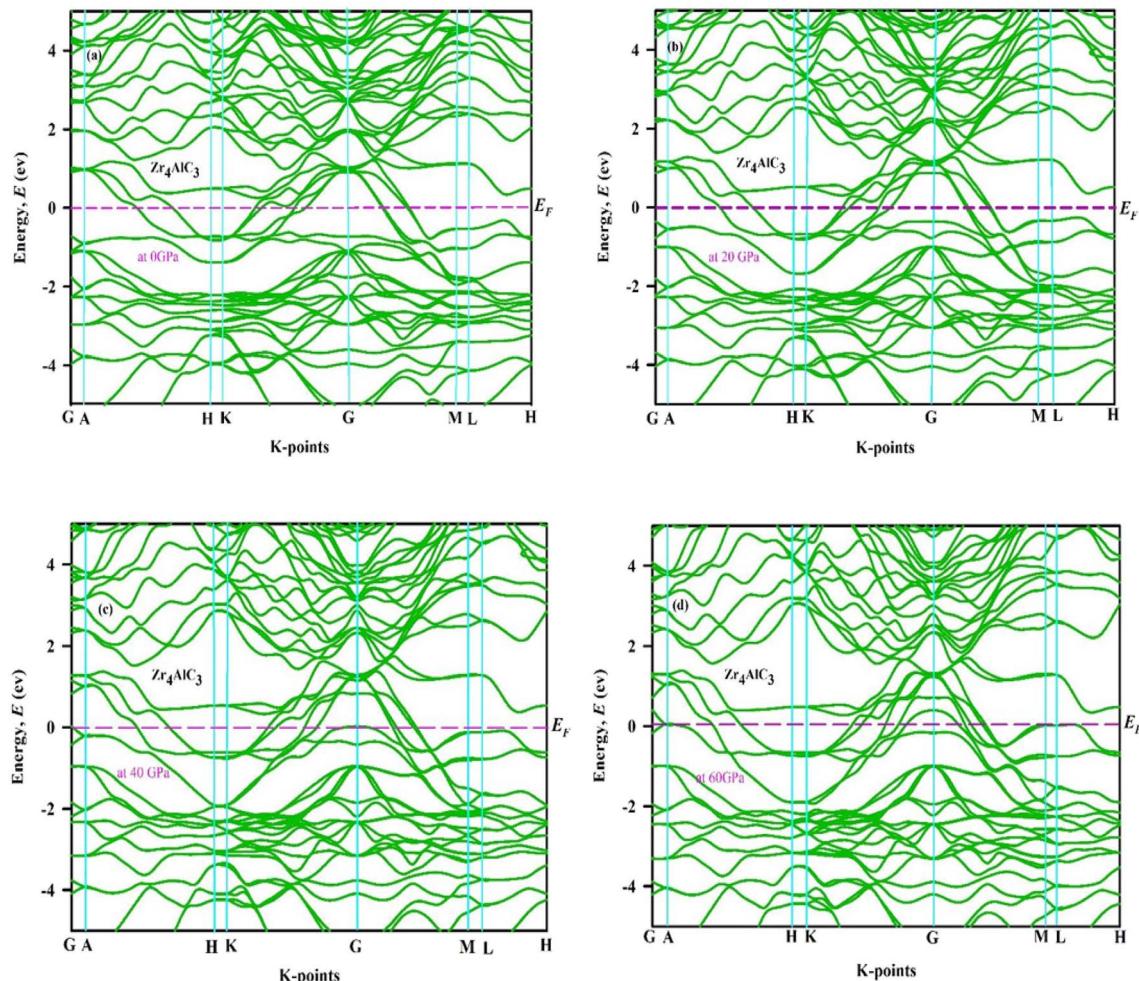
Fig. 11 Electronic band structures of Zr_4AlC_3 at (a) 0, (b) 20, (c) 40, and (d) 60 GPa.
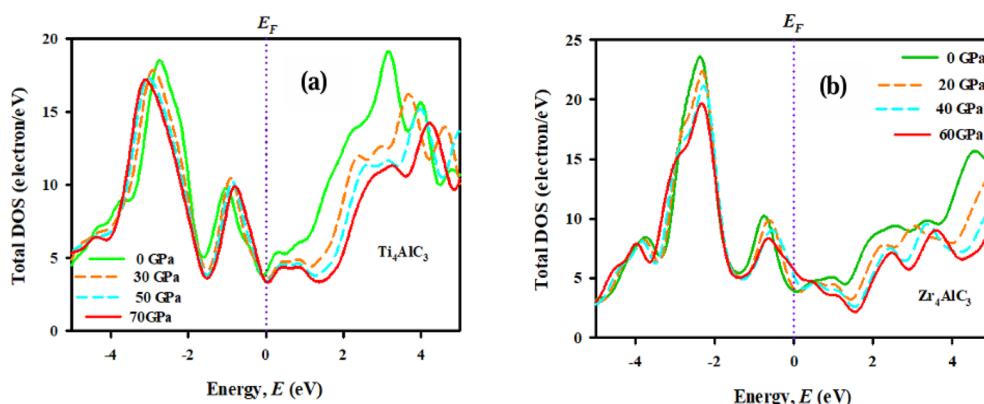

Fig. 12 Total density of states for (a) Ti_4AlC_3 and (b) Zr_4AlC_3 under varying pressures.

function—are crucial for optoelectronic devices like solar cells and LEDs. This work examines Ti_4AlC_3 and Zr_4AlC_3's optical response from 0 to 30 eV under pressure, providing the first theoretical insight into their pressure-dependent behavior for industrial and energy applications. Optical behavior is described by the frequency-dependent dielectric function:

$$\varepsilon(\omega) = \varepsilon_1(\omega) + i\varepsilon_2(\omega) \tag{23}$$

Here, $\varepsilon_1(\omega)$ is the real part of the dielectric function, indicating the material's ability to store electromagnetic energy, while $\varepsilon_2(\omega)$ is the imaginary part, representing energy loss from electronic transitions and absorption. The imaginary part is
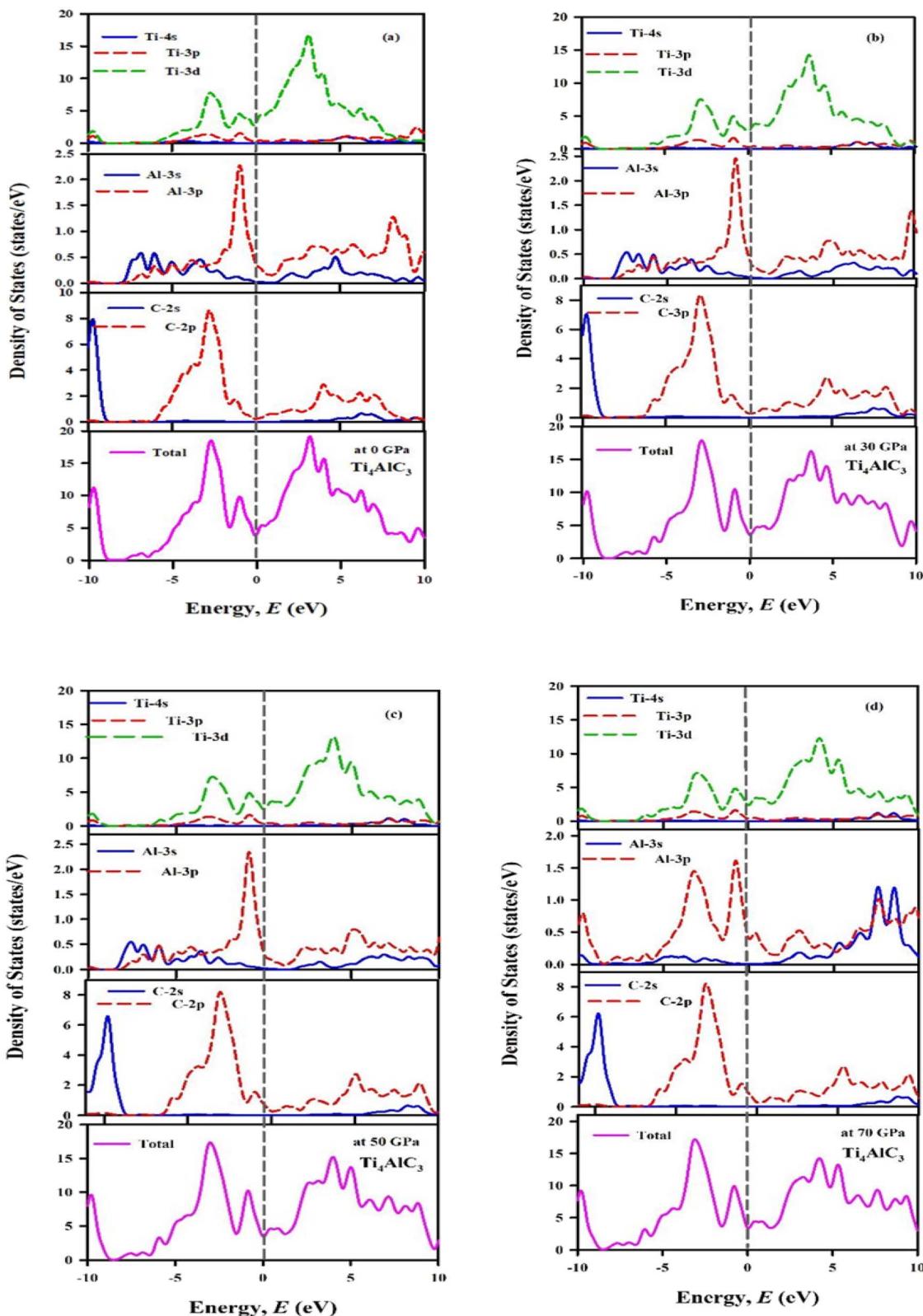
Fig. 13   Partial density of states for Ti$_4$AlC$_3$ at (a) 0, (b) 30, (c) 50, and (d) 70 GPa.

calculated using momentum matrix elements considering all transitions between occupied and unoccupied states, as expressed by the following equation.[89,90]

$$\varepsilon_2(\omega) = \frac{2e^2\pi}{\Omega\varepsilon_0}\sum_{k,v,c}|\psi_k^{\ c}|u \times r|\psi_k^{\ v}|^2\delta(E_k^{\ c} - E_k^{\ v} - E) \quad (24)$$
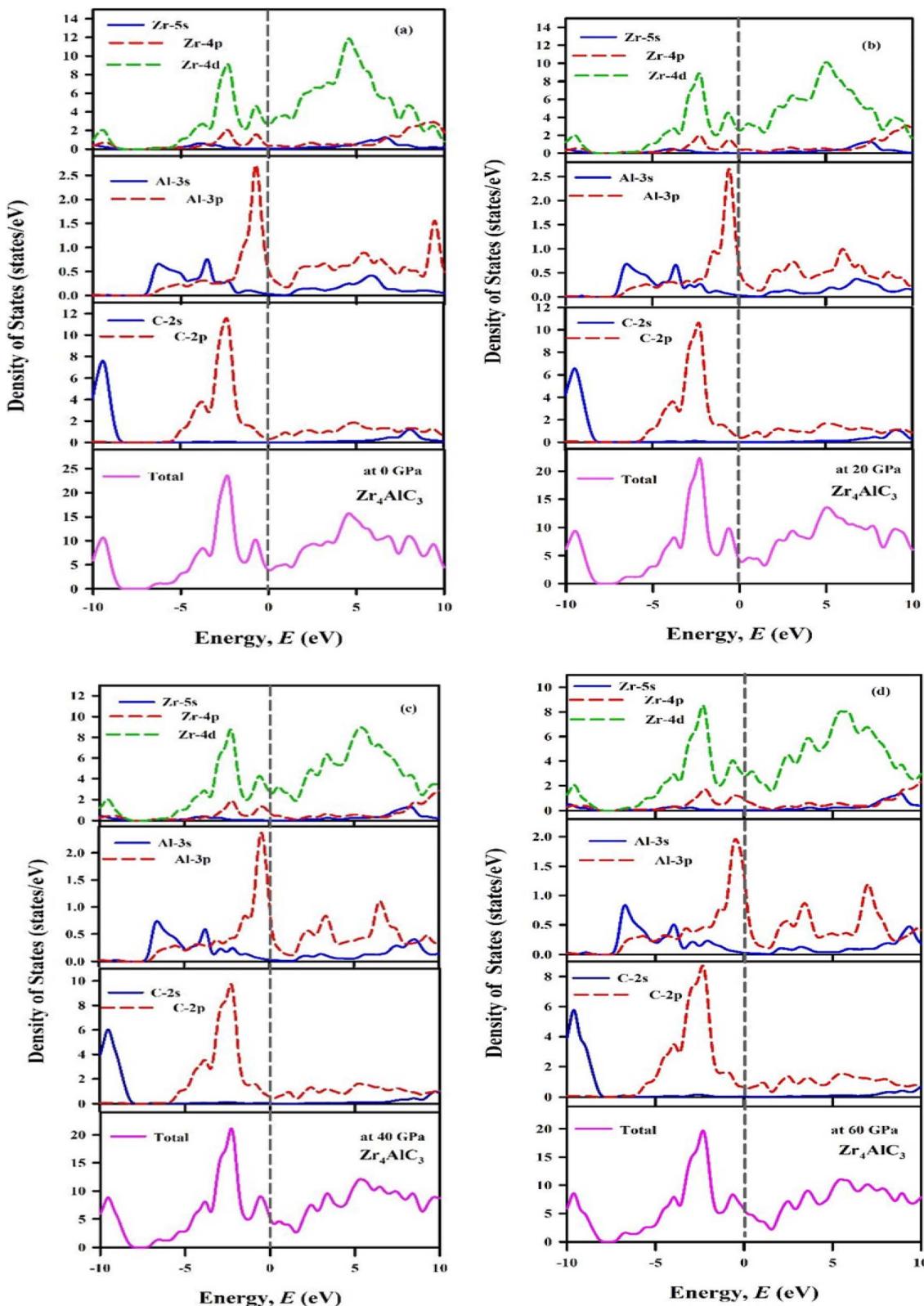
Fig. 14 Partial density of states for Zr_4AlC_3 at (a) 0, (b) 20, (c) 40, and (d) 60 GPa.

In this equation, the integral spans the first Brillouin zone. Here, **u** is the polarization vector of the incident electric field, ω the light frequency, e the electronic charge, and ψ_k^c and ψ_k^v the conduction and valence band wave functions at k-point k. The real part, $\varepsilon_1(\omega)$, is derived using the Kramers–Kronig relation.[91,92]

Table 7 Mulliken atomic populations of M_4AlC_3 (M = Ti, Zr) under various pressure

Compounds	Pressure, P (GPa)	Species	s	p	d	Total	Charge	Bond	Population	Length (Å)
Ti$_4$AlC$_3$	0	C	1.47	3.20	0	4.67	−0.67	C–Ti	1.22	2.06
		Al	1.07	1.95	0	3.03	−0.03	—	—	—
		Ti	2.13	6.61	2.63	11.36	0.64	—	—	—
	20	C	1.46	3.21	0	4.67	−0.67	C–Ti	1.16	2.01
		Al	1.00	2.01	0	3.01	−0.01	—	—	—
		Ti	2.09	6.60	2.67	11.37	0.63	—	—	—
	40	C	1.45	3.22	0	4.67	−0.67	C–Ti	1.11	1.98
		Al	0.97	2.04	0	3.01	−0.01	—	—	—
		Ti	2.07	6.59	2.71	11.37	0.63	—	—	—
		C	1.44	3.22	0	4.67	−0.67	C–Ti	1.03	1.95
		Al	0.94	2.08	0	3.02	−0.02	—	—	—
		Ti	2.03	6.57	2.77	11.37	0.63	—	—	—
Zr$_4$AlC$_3$	0	C	1.50	3.26	0	4.76	−0.76	C–Zr	1.26	2.24
		Al	1.14	1.92	0	3.05	−0.05	—	—	—
		Zr	2.19	6.47	2.62	11.27	0.73	—	—	—
	20	C	1.49	3.27	0	4.76	−0.76	C–Zr	1.18	2.19
		Al	1.07	1.97	0	3.04	−0.04	—	—	—
		Zr	2.15	6.43	2.68	11.27	0.73	—	—	—
	40	C	1.49	3.28	0	4.77	−0.77	C–Zr	1.11	2.15
		Al	1.04	2.00	0	3.03	−0.03	—	—	—
		Zr	2.13	6.40	2.74	11.26	0.74	—	—	—
	60	C	1.49	3.28	0	4.71	−0.77	C–Zr	1.03	2.13
		Al	1.02	1.98	0	3.00	−0.0	Al–Zr	0.31	2.67
		Zr	2.10	6.36	2.79	11.26	0.74	—	—	—

$$\varepsilon_1(\omega) = 1 + \frac{2}{\pi} M \int_0^\infty \frac{\omega' \varepsilon_2(\omega')}{\omega'^2 - \omega^2} d\omega' \quad (25)$$

The integral is denoted as M. From the complex dielectric function $\varepsilon_2(\omega)$, key optical parameters—refractive index $n_1(\omega)$, absorption coefficient $\alpha(\omega)$, reflectivity $R(\omega)$, and energy loss spectrum $L(\omega)$—are derived using the following relations:[92,93]

$$n(\omega) = \left[\sqrt{\varepsilon_1{}^2(\omega) + \varepsilon_2{}^2(\omega)} + \varepsilon_1(\omega) \right]^{1/2} \Big/ \sqrt{2} \quad (26)$$

$$k(\omega) = \left[\sqrt{\varepsilon_1{}^2(\omega) + \varepsilon_2{}^2(\omega)} - \varepsilon_1(\omega) \right]^{1/2} \Big/ \sqrt{2} \quad (27)$$

$$\alpha(\omega) = \sqrt{2}\omega \left[\sqrt{\varepsilon_1{}^2(\omega) + \varepsilon_2{}^2(\omega)} - \varepsilon_1(\omega) \right]^{1/2} \quad (28)$$

$$\sigma(\omega) = \frac{\omega \varepsilon_2}{4\pi} \quad (29)$$

$$R(\omega) = \left| \frac{\left(\varepsilon(\omega)^{1/2} - 1 \right)}{\left(\varepsilon(\omega)^{1/2} + 1 \right)} \right|^2 \quad (30)$$

$$L(\omega) = \frac{\varepsilon_2(\omega)}{\varepsilon_1{}^2(\omega) + \varepsilon_2{}^2(\omega)} \quad (31)$$

A Gaussian smearing of 0.5 eV was applied in all optical calculations for accuracy and smooth spectra. For metallic Ti$_4$AlC$_3$ and Zr$_4$AlC$_3$, both inter- and intra-band transitions

impact the dielectric function. A Drude term with a 4 eV plasma frequency and 0.05 eV damping was used to model free-electron effects, improving low-energy optical response.[94] The dielectric function, a key optical property, refer to in what way a material reacts to an exterior electromagnetic (EM) field. It has two components: the real part, specifying the material's capability to store electric energy, whereas imaginary part, related to energy absorption and dissipation. For M_4AlC_3 (M = Ti, Zr) compounds, both components were analyzed under varying pressure and plotted in Fig. 16(a, b) as functions of photon energy. At low energies, the negative real part confirms their metallic nature. As energy increases, $\varepsilon_1(\omega)$ becomes positive, peaks, then decreases and turns negative again—demonstrating a Drude-like response typical of metals. This behavior is consistent across all pressures, indicating that both compounds retain their metallicity, which aligns with earlier band structure results. Under pressure, distinct peaks appear in the dielectric function: for Zr$_4$AlC$_3$ between 2.21–2.35 eV (0–60 GPa) and for Ti$_4$AlC$_3$ between 1.6–2.52 eV (0–70 GPa), all within the visible range. This confirms their sustained optical activity under pressure, highlighting potential for applications in optical coatings, sensors, and energy-efficient window technologies. For both compounds, the imaginary part of the dielectric function, $\varepsilon_2(\omega)$, shows a large positive value at low photon energies, indicating strong absorption due to inter-band transitions and free-electron behavior. As photon energy increases, $\varepsilon_2(\omega)$ gradually decreases and approaches zero around 24–26 eV—marking the plasma frequency, where the material transitions from absorption to transparency. At this point, both the absorption coefficient and reflectivity drop sharply. This plasma
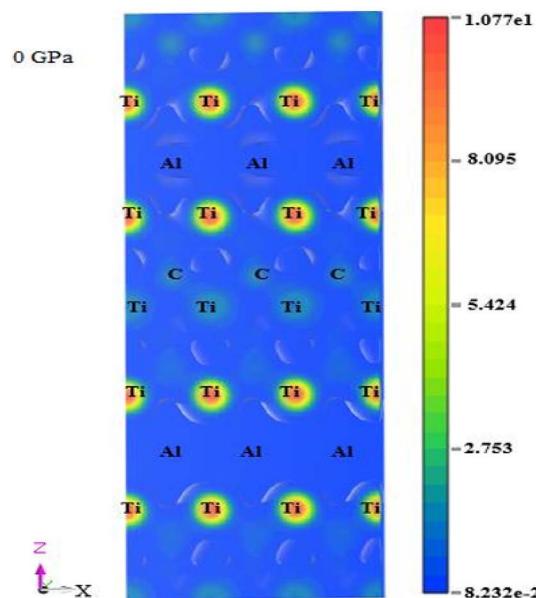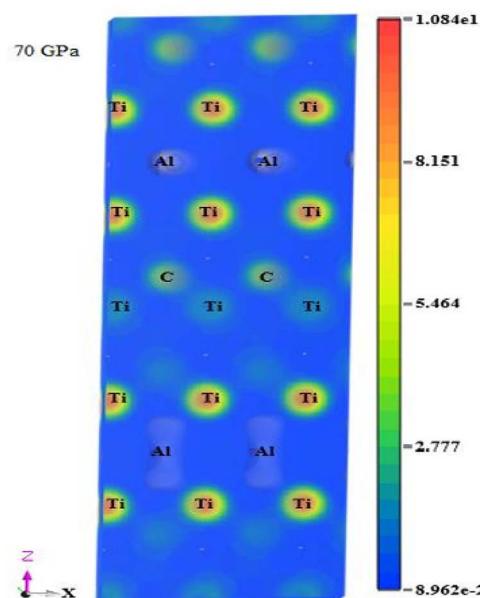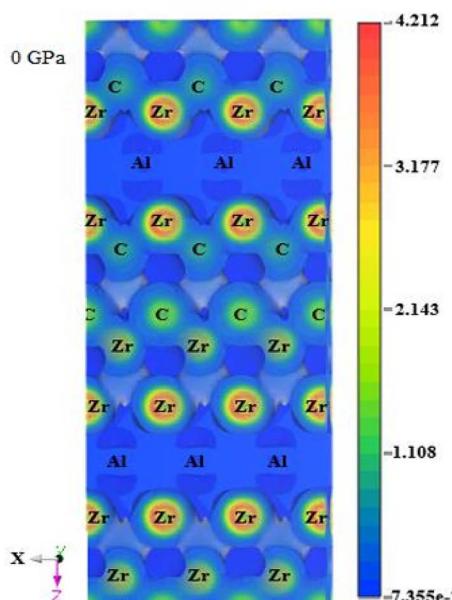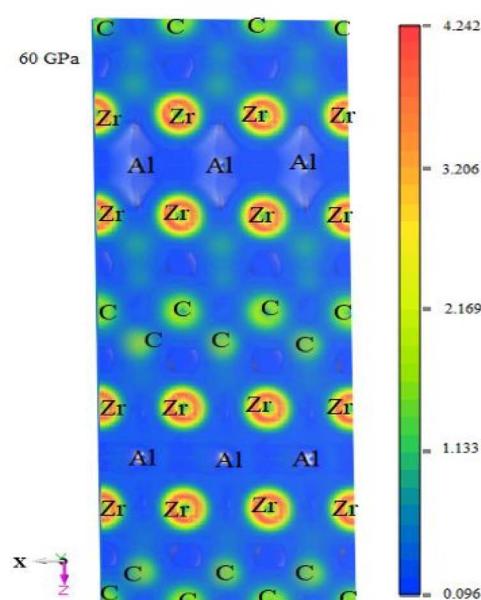
Fig. 15 Electron charge density of Ti_4AlC_3 at (a) 0 GPa, (b) 70 GPa, and Zr_4AlC_3 at (c) 0 GPa, (d) 60 GPa.

frequency is crucial for understanding optical transitions, especially in plasmonic applications, optical coatings, and electromagnetic shielding.

The refractive index, a dimensionless quantity, is the fraction of the speed of light in a vacuum to its speed in a material, indicating how much light slows down and bends upon entering. It is key to understanding optical behaviors like reflection, refraction, and transmission. A higher refractive index indicates that light travels more slowly in the medium.[95] As shown in Fig. 16(c), the refractive indices of M_4AlC_3 (M = Ti,

Zr) under different pressures are notably high in the infrared region, ranging from 3.8 to 5.02. These values suggest strong interaction with infrared light. With increasing pressure, variations in peak values indicate enhanced ability to guide and manipulate infrared light, making these materials promising for optical communication, infrared sensors, fiber optics, and laser systems.

The absorption coefficient $\alpha(\omega)$ measures a material's light absorption efficiency across wavelengths, key for solar and optoelectronic uses. For M_4AlC_3 (M = Ti, Zr), pressure-
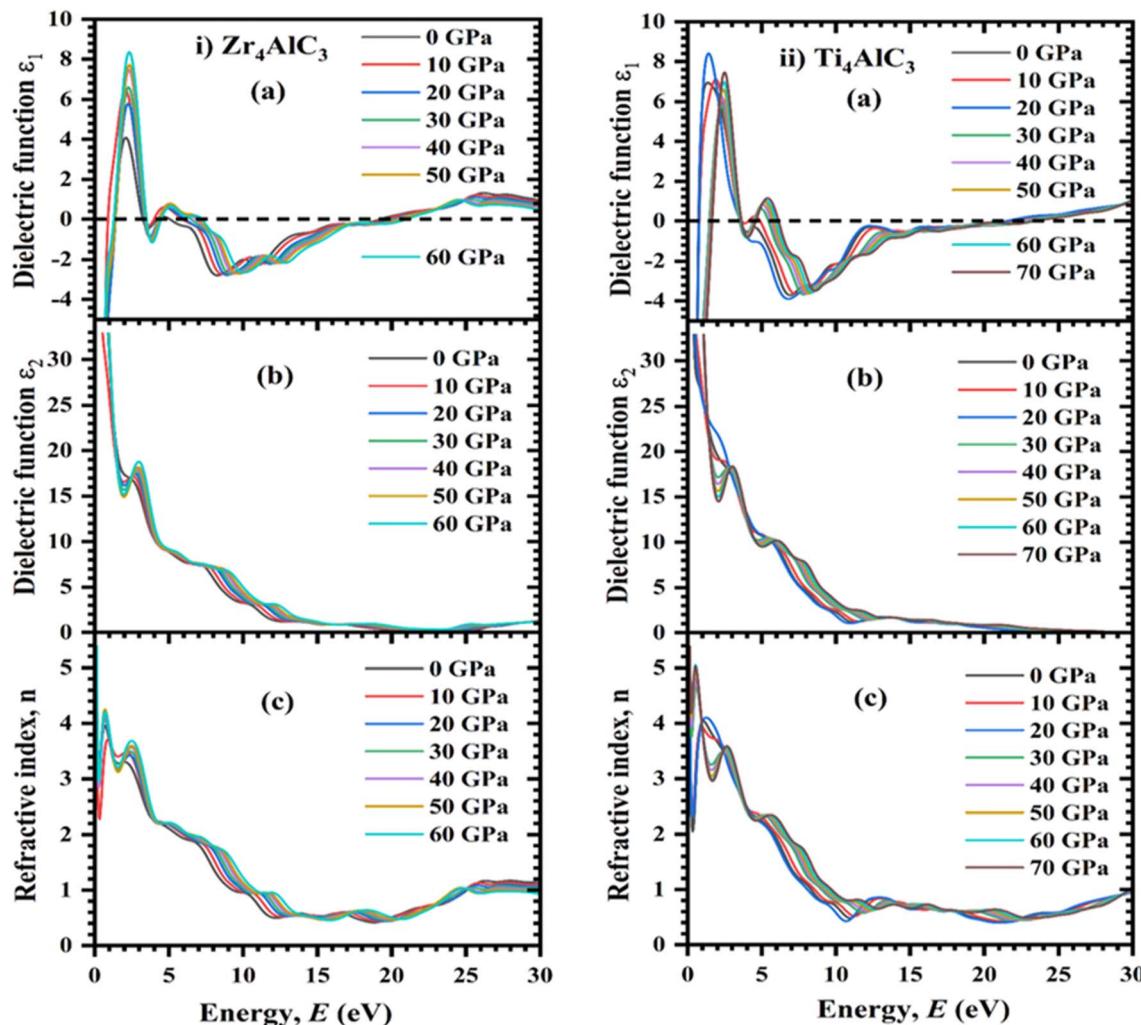
Fig. 16 Pressure-dependent dielectric function of (i) Zr_4AlC_3 and (ii) Ti_4AlC_3: (a) real part, (b) imaginary part, and (c) refractive index.

dependent absorption spectra appear in Fig. 17(a) for Ti_4AlC_3 and Fig. 18(a) for Zr_4AlC_3. Absorption starts at zero in low photon energies, confirming metallicity, rises through the infrared and visible regions, and peaks sharply in the UV range. For Ti_4AlC_3, peaks appeared between 7.78–8.51 eV (at 0–70 GPa), while for Zr_4AlC_3, peaks occurred between 10.93–12.74 eV (0–60 GPa). Notably, maximum absorption coincides with minima in reflectivity and energy loss, indicating high efficiency in light absorption. This makes both compounds strong candidates for UV optoelectronic applications such as UV sensors, LEDs, photodetectors, and optical communication systems where effective UV light control is essential.

Optical conductivity reflects how photon excitation increases a material's electrical conductivity.[96,97] The real part, $\sigma(\omega)$, *versus* photon energy under pressure is shown in Fig. 17(b) for Ti_4AlC_3 and Fig. 18(c) for Zr_4AlC_3. In both, $\sigma(\omega)$ starts at zero energy, indicating overlapping valence and conduction bands at the Fermi level, confirming their metallic nature and lack of band gap, consistent with band structure results. This allows continuous electron excitation, enabling photocurrent generation across a wide energy range—ideal for photodetectors and

photovoltaic devices. For Ti_4AlC_3, major conductivity peaks appear between 5.92–6.41 eV (0–70 GPa), while for Zr_4AlC_3, peaks lie between 7.25–9.02 eV (0–60 GPa). With increasing pressure, both peak intensity and position shift upward. Notably, conductivity minima align with the lowest absorption points. Since the peaks fall in the UV range, both materials demonstrate strong potential for UV optoelectronic applications like sensors, LEDs, and photodetectors.

Reflectivity is a crucial optical property for evaluating the practical applications of MAX phase materials. The reflectivity spectra, $R(\omega)$, under pressure are shown in Fig. 17(d) for Ti_4AlC_3 and Fig. 18(d) for Zr_4AlC_3, illustrating how reflectivity varies with photon energy. This analysis helps determine the suitability of M_4AlC_3 (M = Ti, Zr) as protective coatings for minimizing solar heat absorption. According to Li *et al.*,[98] a reflectivity of at least 44% is required for effective thermal barrier coatings (TBCs). Both compounds show reflectivity around 60%, indicating strong potential for such applications. The highest reflectivity is observed in the infrared region, confirming their effectiveness in reflecting low-energy radiation and reducing heat absorption. In contrast, reflectivity decreases
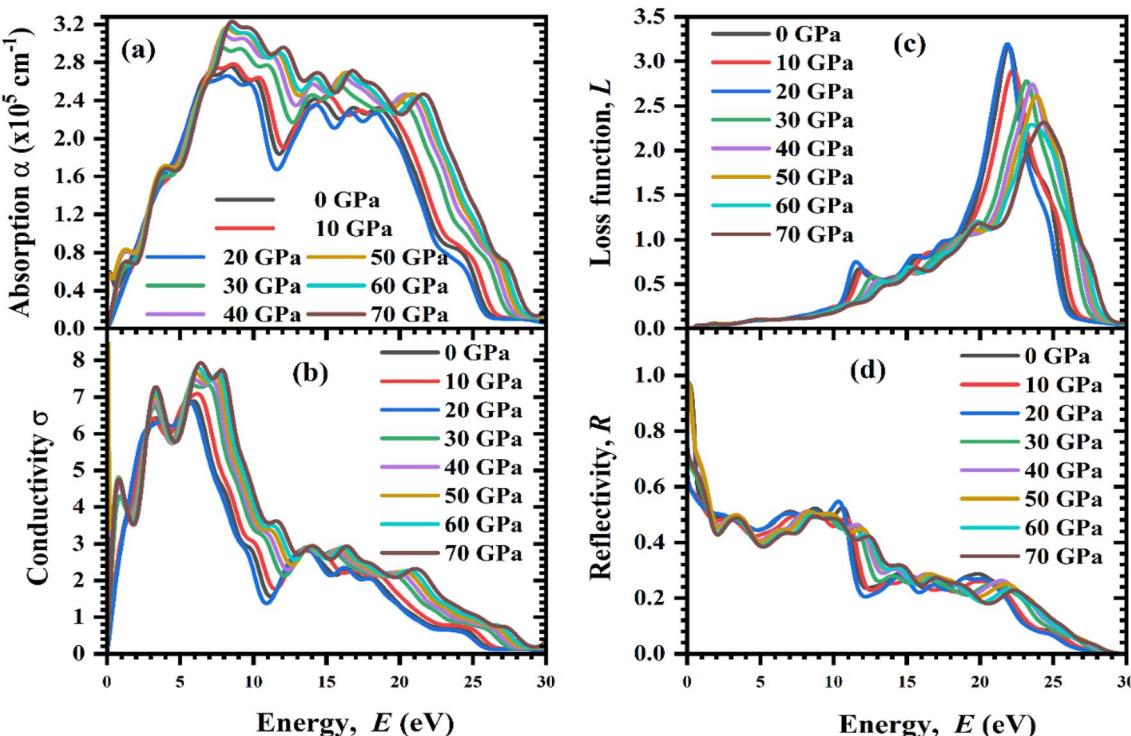
Fig. 17 Pressure-dependent (a) absorption, (b) loss function, (c) conductivity, and (d) reflectivity of Ti$_4$AlC$_3$.

in the visible range, while small peaks appear in the UV region—between 7–10 eV for Ti$_4$AlC$_3$ and 9–13 eV for Zr$_4$AlC$_3$. Overall, their high infrared reflectivity makes them promising candidates for use in aerospace coatings, energy-efficient building materials, and high-temperature industrial protection.

The electron energy loss function, $L(\omega)$, describes the energy lost by fast-moving electrons as they pass through a material
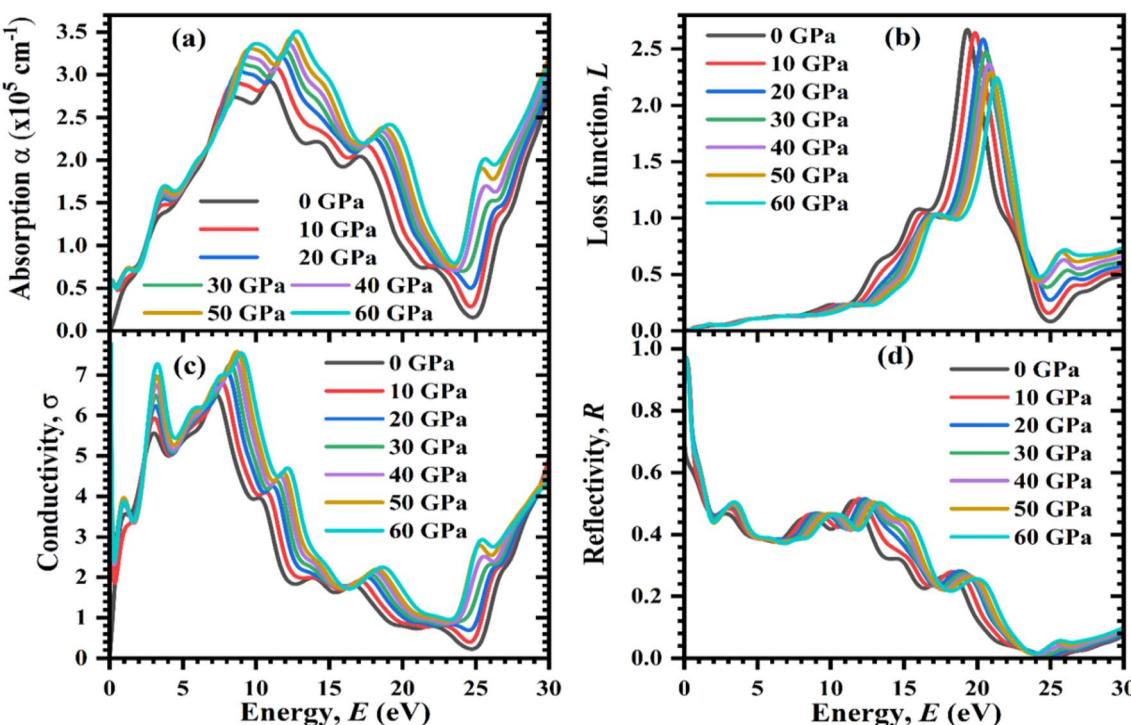
Fig. 18 Pressure dependent (a) absorption, (b) loss function, (c) conductivity and (d) reflectivity of Zr$_4$AlC$_3$ compound.

© 2025 The Author(s). Published by the Royal Society of Chemistry

and provides insight into electron-material interactions.[99] Fig. 17(c) and **18(b)** show the loss spectra of Ti_4AlC_3 and Zr_4AlC_3 under pressure. In the 0–15 eV range, no distinct peaks are observed, indicating the absence of significant plasmonic excitations and minimal energy dissipation—suggesting a stable electronic response, which is advantageous for devices requiring efficient charge transport and low electron scattering. The most prominent energy loss occurs at the plasma frequency, where $\varepsilon_1(\omega) = 0$ and $\varepsilon_2(\omega) < 1$, as seen in the dielectric function analysis.[100] In both materials, peaks in the loss function appear between 19–25 eV, corresponding to sharp decreases in reflectivity, absorption, and conductivity. Beyond this energy, the materials become transparent. This transparency above the plasma frequency highlights their potential for UV optics, transparent conductive coatings, and high-frequency optoelectronic devices.

3.6 Thermodynamic properties

MAX phase compounds, valued for their strength, toughness, and thermal stability, are promising for high-temperature applications. Studying their thermal properties is essential to assess performance and limits. The Debye temperature (θ_D) reflects the highest atomic vibrational mode and relates to specific heat, melting point, and thermal expansion.[52] Anderson's method, a reliable and simple approach, calculates θ_D using the average elastic (sound) wave velocity as follows:[101]

$$\theta_D = \frac{h}{k_B}\left[\left(\frac{3n}{4\pi}\right)\frac{N_A\rho}{M}\right]^{1/3} \times v_m \tag{32}$$

In this equation, h, k_B, N_A are Planck's constant, Boltzmann constant, and Avogadro's number, respectively; ρ and M denote the material's density and molecular weight; n is the number of atoms per unit cell; and v_m is the average sound velocity. The average sound velocity in crystals is calculated as follows:[102]

$$v_m = \left[\frac{1}{3}\left(\frac{2}{v_t^3} + \frac{1}{v_l^3}\right)\right]^{-1/3} \tag{33}$$

Longitudinal (v_l) and transverse (v_t) sound velocities in crystals are calculated from shear (G) and bulk (B) moduli using these formulas:[101]

$$v_l = \left(\frac{3B + 4G}{3\rho}\right)^{1/2} \tag{34}$$

And

$$v_t = \left(\frac{G}{\rho}\right) \tag{35}$$

Table 8 lists density (ρ), transverse (v_t), longitudinal (v_l), average sound velocity (v_m), and Debye temperature (θ_D) for Ti_4AlC_3 and Zr_4AlC_3 under various pressures, with trends shown in Fig. 19 and 20. Both materials' densities rise with pressure due to volume reduction, and v_m follows suit, closely tied to θ_D. Ti_4AlC_3's Debye temperature steadily increases with pressure, while Zr_4AlC_3's stabilizes near 30 GPa, indicating limited further effect on atomic vibrations. Higher θ_D reflects stronger bonding, hardness, and thermal conductivity. Ti_4AlC_3 has significantly higher θ_D highlights its superior bonding and thermal properties, making it ideal for high-performance uses like coatings, thermal management. Also the value of Debye temperature of Ti_4AlC_3 increases with pressure making it

Table 8 Evaluated properties of M_4AlC_3 (M = Ti, Zr) compounds include density (ρ), transverse (v_t) and longitudinal (v_l) sound velocities, average sound velocity (v_m), Debye temperature (θ_D), melting temperature (T_m), and minimum thermal conductivity (k_{min})

| Elements	Pressure (GPa)	ρ (gm/cm³)	v_t (m s⁻¹)	v_l (m s⁻¹)	v_m (m s⁻¹)	θ_D (K)	k_{min} (W m⁻¹ K⁻¹)	T_m (K)	Ref.
Ti_4AlC_3	0	4.453	5762.54	9214.12	5851.94	827.86	1.941	2065.13	This study
Hf_4AlC_3	0	6.926	3684.90	5924.02	—	496.81	1.154	—	34
Nb_4AlC_3	0	6.930	4701.66	7795.24	5382.06	681.78	1.340	2166.18	37
Ti_4AlC_3	0	8.618	5792.27	9054.56	—	837.32	2.070	—	34
	10	4.684	6128.60	9949.42	6190.97	897.02	2.124	2377.50	This study
	20	4.883	6151.38	10 201.43	6227.09	914.91	2.197	2577.72	
	30	5.059	6262.37	10 581.75	6349.64	943.97	2.294	2811.41	
	40	5.221	6382.29	10 882.97	6475.41	972.74	2.389	3018.84	
	50	5.368	6388.60	11 083.19	6491.65	984.21	2.440	3193.34	
	60	5.509	6403.42	11 304.12	6516.15	996.35	2.493	3377.72	
	70	5.643	6474.23	11 501.75	6590.90	1015.03	2.562	3525.15	
Zr_4AlC_3	0	5.929	4522.95	7381.03	4585.33	602.20	1.299	1823.54	
		6.802	4656.61	7455.78	—	623.76	1.434	—	34
Hf_4AlC_3	0	6.926	3684.90	5924.02	—	496.81	1.154	—	
Nb_4AlC_3	0	6.930	4701.66	7795.24	5382.06	681.78	1.340	2166.18	37
Zr_4AlC_3	10	6.262	4705.81	7863.04	4779.98	640.00	1.405	2073.21	This study
	20	6.552	4866.82	8284.01	4950.43	643.52	1.500	2308.62	
	30	6.799	4885.06	8496.33	4978.29	691.71	1.546	2467.73	
	40	7.044	4832.22	8560.48	4932.57	685.52	1.569	2538.36	
	50	7.278	4774.81	8646.28	4882.77	684.11	1.589	2632.71	
	60	7.497	4692.63	8727.11	4809.32	681.86	1.595	2754.26	
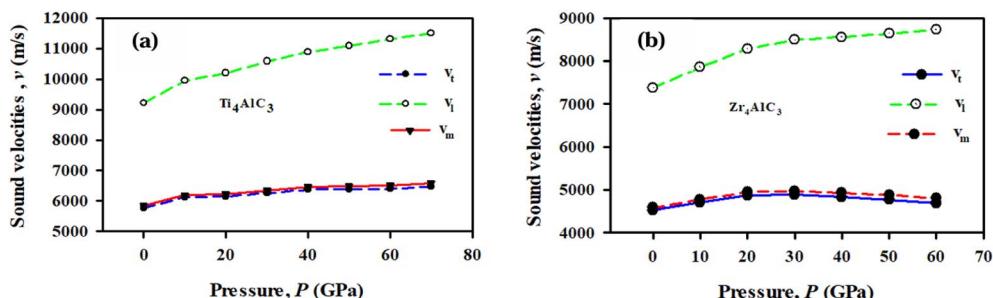
Fig. 19 Evaluated transverse (v_t), longitudinal (v_l), and average (v_m) sound velocities of (a) Ti_4AlC_3 and (b) Zr_4AlC_3 under varying pressure.
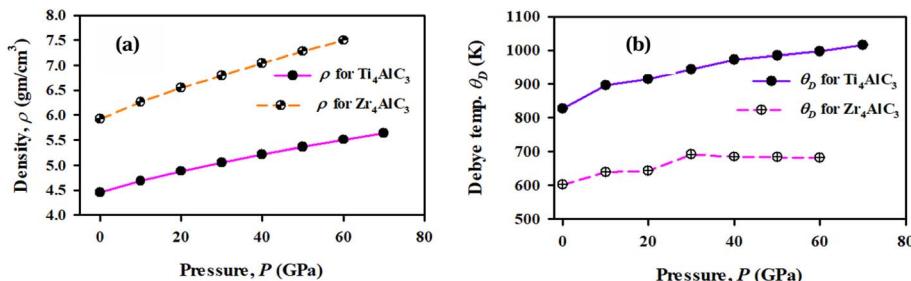

Fig. 20 Calculated (a) density, ρ and (b) Debye temperature, θ_D for Ti_4AlC_3 and Zr_4AlC_3 different pressure.

suitable for application in aerospace engineering technology. According to the value of Debye temperature listed in Table 8, these compounds can be arranged as Ti_4AlC_3 > Nb_4AlC_3 > Zr_4AlC_3 > Hf_4AlC_3.

Minimum thermal conductivity (k_{min}) defines the lowest limit of heat conduction in MAX phases, relevant at extreme temperatures where phonon transport is minimal. It reflects atomic response to thermal variations and is directly linked to average sound velocity (v_m). Higher v_m implies greater k_{min}. It is calculated using the following equation:[103]

$$k_{min} = k_B v_m \left(\frac{n N_A \rho}{M}\right)^{2/3} \tag{36}$$

The symbols in this equation retain the same meanings as defined in eqn (32).

The computed minimum thermal conductivity (k_{min}) values for M_4AlC_3 (M = Ti, Zr) are listed in Table 8, with their pressure-dependent trends shown in Fig. 21(a). At 0 GPa, Ti_4AlC_3 exhibits a k_{min} of 1.94 W m^{-1} K^{-1}, notably higher than Zr_4AlC_3's 1.29 W m^{-1} K^{-1}. With increasing pressure, k_{min} rises significantly—reaching 2.562 W m^{-1} K^{-1} for Ti_4AlC_3 at 70 GPa and 1.595 W m^{-1} K^{-1} for Zr_4AlC_3 at 60 GPa. Across all pressure levels, Ti_4AlC_3 maintains a higher k_{min} than Zr_4AlC_3. Notably, even at 60 GPa, Zr_4AlC_3's k_{min} remains below the ambient value of Ti_4AlC_3. Fig. 21(a) also highlights a steeper increase in Ti_4AlC_3's k_{min} with pressure, suggesting a stronger pressure sensitivity. For thermal barrier coating (TBC) applications, materials with k_{min} ≈ 1.25 W m^{-1} K^{-1} are ideal.[104] While Zr_4AlC_3 exhibits lower thermal conductivity than Ti_4AlC_3 and Nb_4AlC_3 (see Table 8), making it promising for insulation, its increasing k_{min} under pressure limits its suitability for high-pressure environments.
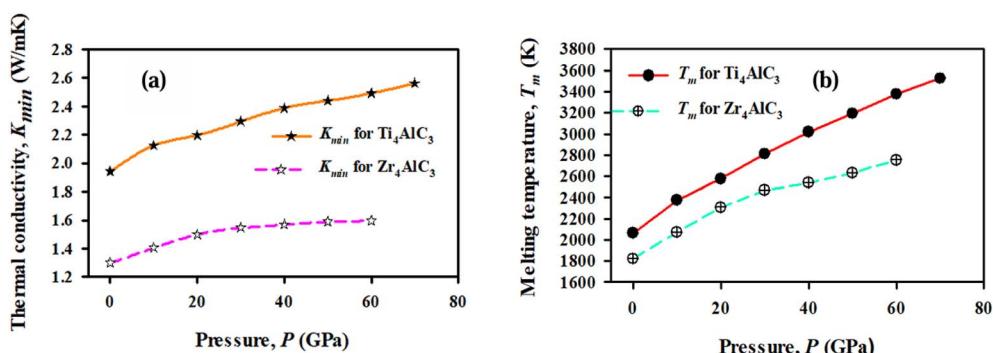

Fig. 21 Calculated (a) minimum thermal conductivity (k_{min}) and (b) melting temperature (T_m) of Ti_4AlC_3 and Zr_4AlC_3 under varying pressure.

Melting temperature (T_m)—the point where a solid becomes liquid at standard pressure—is another key thermal metric. Fine *et al.*[105] proposed an empirical method using elastic constants to estimate the melting point of hexagonal crystals, including MAX phases.

$$T_m = 354 + 1.5\,(2C_{11} + C_{33}) \qquad (37)$$

The calculated melting temperatures of M_4AlC_3 (M = Ti, Zr) at various pressures, presented in Table 8 and Fig. 21(b), show a consistent increase with pressure. As E is closely related with C_{11} and C_{33}, this trend aligns with the rise in Young's modulus (E) discussed in Section 3.2, indicating enhanced structural rigidity under compression. Ti_4AlC_3 exhibits higher melting temperatures than Zr_4AlC_3 across all pressure levels, highlighting its superior thermal resilience. This makes Ti_4AlC_3 more suitable for extreme heat environments such as aerospace and energy systems. While Zr_4AlC_3 remains viable for high-temperature applications, its relatively lower melting point limits its use in more thermally demanding conditions.

4. Conclusions

The structural, mechanical, electrical, thermal, and optical properties of M_4AlC_3 (M = Ti, Zr) MAX phase compounds were investigated under 0–70 GPa pressure using first-principles DFT calculations *via* the CASTEP code. At ambient conditions, computed structural parameters aligned well with previous theoretical and experimental data. With increasing pressure, both lattice parameters and unit cell volumes decreased, while elastic constants (C_{ij}) satisfied Born's criteria, confirming mechanical stability. Pressure enhanced bulk, shear, and Young's moduli, indicating stronger bonding, greater resistance to deformation, and increased stiffness. Pugh's and Poisson's ratios revealed a brittle-to-ductile transition at ~60 GPa for Ti_4AlC_3 and ~40 GPa for Zr_4AlC_3. The machinability index (μ_m) also improved with pressure, especially for Ti_4AlC_3, suggesting better industrial workability, although hardness declined, indicating reduced plastic deformation resistance. Anisotropic indices confirmed high elastic anisotropy under pressure. Electronic band structures and DOS confirmed metallic behavior across the pressure range. Optical properties—including dielectric function, absorption, and conductivity—further supported their metallic nature. High UV absorption and photoconductivity suggest potential for coatings to reduce solar heating and for use in optoelectronic devices, transparent conductive films, and smart windows. Thermal properties such as Debye temperature (Θ_D), minimum thermal conductivity (k_{min}), and melting temperature (T_m) all increased with pressure, indicating stronger bonding and higher thermal resilience. Ti_4AlC_3 consistently outperformed Zr_4AlC_3 in Θ_D and T_m, making it more suitable for extreme thermal environments. Overall, this study offers valuable insights into pressure-tuned behavior of M_4AlC_3 compounds, supporting their potential in high-temperature applications, optoelectronics, UV detection, thermal barrier coatings, and other advanced technologies.

Data availability

Data will be sent on request to the corresponding author Md. Atikur Rahman (atik 0707phy@gmail.com)

Conflicts of interest

The authors ensure that there is no conflict to declare about the publication of this article.

Acknowledgements

References

1 M. W. Barsoum, The $M_{N+1}AX_N$ phases: a new class of solids, *Prog. Solid State Chem.*, 2000, **28**(1–4), 201–281, DOI: **10.1016/s0079-6786(00)00006-6**.

2 M. W. Barsoum, D. Brodkin and T. El-Raghy, Layered machinable ceramics for high temperature applications, *Scr. Mater.*, 1997, **36**(5), 535–541.

3 T. El-Raghy, *et al.*, Processing and mechanical properties of Ti_3SiC_2: II, effect of grain size and deformation temperature, *J. Am. Ceram. Soc.*, 1999, **82**(10), 2855–2860.

4 A. T. Procopio, T. El-Raghy and M. W. Barsoum, Synthesis of Ti_4AlN_3 and Phase Equilibria in the Ti-Al-N System, *Metall. Mater. Trans. A*, 2000, **31**(2), 373–378.

5 A. T. Procopio, M. W. Barsoum and T. El-Raghy, Characterization of Ti_4AlN_3, *Metall. Mater. Trans. A*, 2000, **31**(2), 333–338.

6 P. Finkel, M. W. Barsoum and T. El-Raghy, Low temperature dependencies of the elastic properties of Ti_4AlN_3, $Ti_3Al_{1.1}C_{1.8}$, and Ti_3SiC_2, *J. Appl. Phys.*, 2000, **87**(4), 1701–1703.

7 M. W. Barsoum and T. El-Raghy, Synthesis and characterization of a remarkable ceramic: Ti_3SiC_2, *J. Am. Ceram. Soc.*, 1996, **79**(7), 1953–1956.

8 Z. M. Sun, H. Hashimoto, Z. F. Zhang, S. L. Yang and S. Tada, *Mater. Trans.*, 2006, **47**, 170–174.

9 M. W. Barsoum, *MAX Phases: Properties of Machinable Ternary Carbidesand Nitrides*; Wiley-VCH, Weinheim, Germany, 2013.

10 P. Chakraborty, A. Chakrabarty, A. Dutta and T. Saha-Dasgupta, *Phys. Rev. Mater.*, 2018, **2**, 103605.

11 M. A. Rahman and M. Z. Rahaman, Study on structural, electronic, optical and mechanical properties of MAX phase compounds and applications: Review article, *Am. J. Mod. Phys.*, 2015, **4**(2), 75–91, DOI: **10.11648/j.ajmp.20150402.15**.

12 H. Nowotny, *Solid State Chem.*, 1970, **2**, 27.

13 C. F. Hu, F. Z. Li, J. Zhang, J. M. Wang, J. Y. Wang and Y. C. Zhou, *Scr. Mater.*, 2007, **57**, 893.

14 H. Hogberg, L. Hultman, J. Emmerlich, T. Joelsson, P. Eklund, J. M. Molina-Aldareguia, J. P. Palmquist, O. Wilhelmsson and U. Jansson, *Surf. Coat. Technol.*, 2005, **193**, 6.

15 B. Manoun, S. K. Saxena, T. El-Raghy and M. W. Barsoum, High-pressure x-ray diffraction study of Ta_4AlC_3, *Appl. Phys. Lett.*, 2006, **88**(20), 2004–2007, DOI: 10.1063/1.2202387.

16 D. Horlait, S. Grasso, N. Al Nasiri, P. A. Burr and W. E. Lee, Synthesis and oxidation testing of MAX phase composites in the Cr-Ti-Al-C quaternary system, *J. Am. Ceram. Soc.*, 2016, **99**(2), 682–690, DOI: 10.1111/jace.13962.

17 B. Anasori, J. Halim, J. Lu, C. A. Voigt, L. Hultman and M. W. Barsoum, Mo_2TiAlC_2: A new ordered layered ternary carbide, *Scr. Mater.*, 2015, **101**, 5–7, DOI: 10.1016/j.scriptamat.2014.12.024.

18 G. Qing-He, X. Zhi-Jun, T. Ling, Z. Xianjun, J. Guozhu, L. Du An, G. Rong-Feng and Y.-J. Yun-Dong, Evidence of the stability of Mo_2TiAlC_2 from first principles calculations and its thermodynamical and optical properties, *Comput. Mater. Sci.*, 2016, **118**, 77–86, DOI: 10.1016/j.commatsci.2016.03.010.

19 M. A. Hadi, R. V. Vovk and A. Chroneos, Physical properties of the recently discovered $Zr_2(Al_{1-x}Bi_x)C$ MAX phases, *J. Mater. Sci.: Mater. Electron.*, 2016, **27**(11), 11925–11933, DOI: 10.1007/s10854-016-5338-z.

20 W. Jeitschko, H. Nowotny and F. Benesovsky, Carbonaceous ternary compounds (H phase), *Monatsh. Chem.*, 1963, **94**(4), 672–676, DOI: 10.1007/BF00913068.

21 M. S. Hossain, M. A. Ali, M. M. Hossain and M. M. Uddin, Physical properties of predicted MAX phase borides Hf_2AB (A =Pb, Bi): a DFT insight, *Mater. Today Commun.*, 2021, **27**, 102411, DOI: 10.1016/j.mtcomm.2021.102411.

22 R. Khatun, M. A. Rahman, K. M. Hossain, M. Z. Hasan, M. Rasheduzzaman and S. Sarker, Physical properties of MAX phase Zr_2PbC under pressure: investigation via DFT scheme, *Phys. B*, 2021, **620**, 413258, DOI: 10.1016/j.physb.2021.413258.

23 S. Sarker, M. A. Rahman and R. Khatun, Study of structural, elastic, electronics, optical and thermodynamic properties of Hf_2PbC under pressure by ab-initio method, *Comput. Condens. Matter*, 2021, **26**, e00512.

24 M. W. Barsoum, The MN+ 1AXN phases: A new class of solids: Thermodynamically stable nanolaminates, *Prog. Solid State Chem.*, 2000, **28**(1–4), 201–281.

25 H. Högberg, L. Hultman, J. Emmerlich, T. Joelsson, P. Eklund, J. M. Molina-Aldareguia, J.-P. Palmquist, O. Wilhelmsson and U. Jansson, Growth and characterization of MAX-phase thin films, *Surf. Coat. Technol.*, 2005, **193**(1–3), 6–10, DOI: 10.1016/j.surfcoat.2004.08.174.

26 J. P. Palmquist, S. Li, P. O. Å. Persson, J. Emmerlich, O. Wilhelmsson, H. Högberg, M. I. Katsnelson, B. Johansson, R. Ahuja, O. Eriksson, L. Hultman and U. Jansson, Mn+ 1AXn phases in the Ti-Si-C system studied by thin-film synthesis and ab initio calculations,

Phys. Rev. B: Condens. Matter Mater. Phys., 2004, **70**(16), 1–13, DOI: 10.1103/PhysRevB.70.165401.

27 J. P. Palmquist, T. El-Raghy, J. Howing, O. Wilhemsson and M. Sundberg, *M2006 Conference of Advanced Ceram & Composites (Abstract No. ICACC-S1-184)*, 2006.

28 C. Hu, Z. Lin, L. He, Y. Bao, J. Wang, M. Li and Y. Zhou, Physical and mechanical properties of bulk Ta_4AlC_3 ceramic prepared by an in situ reaction synthesis/hot-pressing method, *J. Am. Ceram. Soc.*, 2007, **90**(8), 2542–2548, DOI: 10.1111/j.1551-2916.2007.01804.x.

29 P. Eklund, *et al.*, Ta_4AlC_3: Phase determination, polymorphism and deformation, *Acta Mater.*, 2007, **55**(14), 4723–4729, DOI: 10.1016/j.actamat.2007.04.040.

30 C. Hu, F. Li, J. Zhang, J. Wang, J. Wang and Y. Zhou, Nb_4AlC_3: a new compound belonging to the MAX phases, *Scr. Mater.*, 2007, **57**(10), 893–896, DOI: 10.1016/j.scriptamat.2007.07.038.

31 C. J. Rawn, M. W. Barsoum, T. El-Raghy, A. Procipio, C. M. Hoffmann and C. R. Hubbard, Structure of Ti_4AlN_3 - a layered Mn+1AXn nitride, *Mater. Res. Bull.*, 2000, **35**(11), 1785–1796, DOI: 10.1016/S0025-5408(00)00383-4.

32 Z. Li, Y. Zhang, K. Wang, Z. Wang, G. Ma, P. Ke and A. Wang, Highly dense passivation enhanced corrosion resistance of Ti_2AlC MAX phase coating in 3.5 wt.% NaCl solution, *Corros. Sci.*, 2024, **228**, 111820.

33 Z. Li, Z. Wang, G. Ma, R. Chen, W. Yang, K. Wang, P. Ke and A. Wang, High-performance Cr_2AlC MAX phase coatings for ATF application: Interface design and oxidation mechanism, *Corros. Commun.*, 2024, **13**, 27–36.

34 A.-L. Ding, C.-M. Li, J. Wang, J. Ao, F. Li and Z.-Q. Chen, Anisotropy of elasticity and minimum thermal conductivity of monocrystal M4AlC3 (M= Ti, Zr, Hf), *Chin. Phys. B*, 2014, **23**(9), 096201.

35 C. Li and Z. Wang, First-principles study of structural, electronic, and mechanical properties of the nanolaminate compound Ti_4GeC_3 under pressure, *J. Appl. Phys.*, 2010, **107**(12), 123511.

36 R. Khatun, A. Rahman, D. C. Roy, A. A. Khatun, M. Hossain, U. Rani, P. K. Kamlesh, A. Irfan and S. C. Mouna, DFT study on the structural, mechanical, electronic, optical and thermodynamic properties of recently synthesized MAX Phase compounds A_3InC_2 (A= Zr, Hf) under ambient and elevated pressure, *Mater. Today Commun.*, 2024, **40**, 109964.

37 M. Nishat, M. A. Rahman, M. F. Islam, M. A. Hasnat, F. Ahmed and M. Z. Hasan, Pressure effect on the physical properties of 413-type MAX phase compound Nb_4AlC_3: Insights from DFT simulation, *Mater. Sci. Eng., B*, 2024, **299**, 116940.

38 J. P. Perdew, K. Burke and M. Ernzerhof, Generalized gradient approximation made simple, *Phys. Rev. Lett.*, 1996, **77**(18), 3865.

39 P. Hohenberg and W. Kohn, Density functional theory (DFT), *Phys. Rev.*, 1964, **136**, B864.

40 M. D. Segall, *et al.*, First-principles simulation: ideas, illustrations and the CASTEP code, *J. Phys.: Condens. Matter*, 2002, **14**(11), 2717.

41 D. Vanderbilt, Soft self-consistent pseudopotentials in a generalized eigenvalue formalism, *Phys. Rev. B: Condens. Matter Mater. Phys.*, 1990, **41**(11), 7892.

42 T. H. Fischer and J. A. lmlof, *J. Phys. Chem.*, 1992, **96**, 768.

43 B. G. Pfrommer, M. Côté, S. G. Louie and M. L. Cohen, Relaxation of crystals with the quasi-Newton method, *J. Comput. Phys.*, 1997, **131**(1), 233–240.

44 R. Hill, The elastic behaviour of a crystalline aggregate, *Proc. Phys. Soc., London, Sect. A*, 1952, **65**(5), 349.

45 Y. Pan, Y. Lin, G. Liu and J. Zhang, Influence of transition metal on the mechanical and thermodynamic properties of IrAl thermal barrier coating, *Vacuum*, 2020, **174**, 109203.

46 G. Ding, F. Zhou, Z. Zhang, Z.-M. Yu and X. Wang, Charge-two Weyl phonons with type-III dispersion, *Phys. Rev.*, 2022, **B105**, 134303.

47 J. Wang and Y. Zhou, Dependence of elastic stiffness on electronic band structure of nanolaminate M_2AlC (M= Ti, V, Nb, and Cr) ceramics, *Phys. Rev. B: Condens. Matter Mater. Phys.*, 2004, **69**(21), 214111.

48 R. Sa, Y. Wei, W. Zha and D. Liu, A first-principle study of the structural, mechanical, electronic and optical properties of vacancy-ordered double perovskite Cs_2TeX_6 (X= Cl, Br, I), *Chem. Phys. Lett.*, 2020, **754**, 137538.

49 M.-M. Wu, *et al.*, First-principles study of elastic and electronic properties of $MgZn_2$ and $ScZn_2$ phases in Mg–Sc–Zn alloy, *J. Alloys Compd.*, 2010, **506**(1), 412–417.

50 G. Surucu, A. Gencer, X. Wang and O. Surucu, Lattice dynamical and thermo-elastic properties of M_2AlB (M =V, Nb, Ta) MAX phase borides, *J. Alloys Compd.*, 2020, **819**, 153256, DOI: **10.1016/j.jallcom.2019.153256**.

51 M. Born, On the stability of crystal lattices. I, *Math. Proc. Cambridge Philos. Soc.*, 1940, **36**(2), 160–172, DOI: **10.1017/S0305004100017138**.

52 X. Luo and B. Wang, Structural and elastic properties of $LaAlO_3$ from first-principles calculations, *J. Appl. Phys.*, 2008, **104**(7), DOI: **10.1063/1.2990068**.

53 M. Fodil, S. Bentata, B. Soudini and D. Rached, Structural and elastic properties of TiN and AlN compounds: first-principles study, *Mater. Sci.-Pol.*, 2014, **32**(2), 220–227, DOI: **10.2478/s13536-013-0184-7**.

54 M. Radjai, N. Guechi and D. Maouche, An ab initio study of structural, elastic and electronic properties of hexagonal MAuGe (M = Lu, Sc) compounds, *Condens. Matter Phys.*, 2021, **24**(1), 13706. **https://arxiv.org/abs/2103.15579**.

55 F. Mouhat and F. X. Coudert, Necessary and sufficient elastic stability conditions in various crystal systems, *Phys. Rev. B: Condens. Matter Mater. Phys.*, 2014, **90**(22), 224104, DOI: **10.1103/PhysRevB.90.224104**.

56 S. K. Mitro, M. A. Hadi, F. Parvin, R. Majumder, S. H. Naqib and A. K. M. A. Islama, Effect of boron incorporation into the carbon-site in Nb_2SC MAX phase: Insights from DFT, *J. Mater. Res. Technol.*, 2021, **11**, 1969–1981, DOI: **10.1016/j.jmrt.2021.02.031**.

57 S. H. Jhi, J. Ihm, S. G. Loule and M. L. Cohen, Electronic mechanism of hardness enhancement in transition-metal carbonitrides, *Nature*, 1999, **399**(6732), 132–134, DOI: **10.1038/20148**.

58 A. Reuss, Calculation of the flow limit of mixed crystals based on the plasticity condition for single crystals, *J. Appl. Math. Mech.*, 1929, **9**(1), 49–58, DOI: **10.1002/zamm.19290090104**.

59 R. Hill, The elastic behaviour of a crystalline aggregate, *Proc. Phys. Soc., London, Sect. A*, 1952, **65**(5), 349–354, DOI: **10.1088/0370-1298/65/5/307**.

60 Z. Sun, D. Music, R. Ahuja and J. M. Schneider, Theoretical investigation of the bonding and elastic properties of nanolayered ternary nitrides, *Phys. Rev. B: Condens. Matter Mater. Phys.*, 2005, **71**(19), 193402.

61 M. Jubair, A. M. M. Tanveer Karim, M. Nuruzzaman, M. Roknuzzaman and M. A. K. Zilani, Pressure dependent structural, elastic and mechanical properties with ground state electronic and optical properties of half-metallic Heusler compounds Cr_2YAl (Y=Mn, Co): first-principles study, *Heliyon*, 2021, **7**(12), e08585; M. M. Hossain, M. A. Ali, M. M. Uddin, M. A. Hossain, M. Rasadujjaman, S. H. Naqib, M. Nagao, S. Watauchi and I. Tanaka, Influence of Se doping on recently synthesized $NaInS_{2-x}Se_x$ solid solutions for potential thermo-mechanical applications studied via first-principles method, *Mater. Today Commun.*, 2021, **26**, 101988, DOI: **10.1016/j.mtcomm.2020.101988**.

62 O. L. Anderson and H. H. Demarest Jr, Elastic constants of the central force model for cubic structures: polycrystalline aggregates and instabilities, *J. Geophys. Res.*, 1971, **76**(5), 1349–1369, DOI: **10.1029/JB076i005p01349**.

63 S. Huang, R. Li, S. T. Qi, B. Chen and J. Shen, A theoretical study of the elastic and thermal properties of ScRu compound under pressure, *Phys. Scr.*, 2014, **89**, 065702.

64 P. Taylor and S. F. Pugh, XCII. Relations between the elastic moduli and the plastic properties of polycrystalline pure metals, *The London, Edinburgh, and Dublin Philosophical Magazine and Journal of Science*, 1954, **45**(367), 823–843.

65 Y. Cao, J. C. Zhu, Y. Liu, Z. S. Nong and Z. H. Lai, First-principles studies of the structural, elastic, electronic and thermal properties of Ni_3Si, *Comput. Mater. Sci.*, 2013, **69**, 40–45.

66 X. Wang, H. Xiang, X. Sun, J. Liu, F. Hou and Y. Zhou, Mechanical properties and damage tolerance of bulk $Yb_3Al_5O_{12}$ ceramic, *J. Mater. Sci. Technol.*, 2015, **31**(4), 369–374, DOI: **10.1016/j.jmst.2015.01.002**.

67 G. Vaitheeswaran, V. Kanchana, A. Svane and A. Delin, Elastic properties of $MgCNi_3$ - a superconducting perovskite, *J. Phys.: Condens. Matter*, 2007, **19**(32), 326214.

68 M. A. Hadi, S. H. Naqib, S. R. G. Christopoulos, A. Chroneos and A. K. M. A. Islam, Mechanical behavior, bonding nature and defect processes of Mo_2ScAlC_2: a new ordered MAX phase, *J. Alloys Compd.*, 2017, **724**, 1167–1175, DOI: **10.1016/j.jallcom.2017.07.110**.

69 O. L. Anderson and H. H. Demarest Jr, Elastic constants of the central force model for cubic structures: polycrystalline aggregates and instabilities, *J. Geophys. Res.*, 1971, **76**(5), 1349–1369, DOI: **10.1029/JB076i005p01349**.

70 X. Zeng, R. Peng, Y. Yu, Z. Hu, Y. Wen and L. Song, Pressure Effect on Elastic Constants and Related Properties of Ti_3Al

Intermetallic Compound: A First-Principles Study, *Materials*, 2018, **11**(10), 2015, DOI: **10.3390/ma11102015**.

71 D. G. Pettifor, Theoretical predictions of structure and related properties of intermetallics, *Mater. Sci. Technol. (United Kingdom)*, 1992, **8**(4), 345–349, DOI: **10.1179/mst.1992.8.4.345**.

72 M. F. Cover, O. Warschkow, M. M. M. Bilek and D. R. McKenzie, A comprehensive survey of M_2AX phase elastic properties, *J. Phys.: Condens. Matter*, 2009, **21**(30), 305403.

73 F. Ernst and M. Rühle, *High-resolution Imaging and Spectrometry of Materials*, 2003, vol. 6, iss. 6, DOI: **10.1016/s1369-7021(03)00637-0**.

74 M. A. Hadi, S. R. G. Christopoulos, S. H. Naqib, A. Chroneos, M. E. Fitzpatrick and A. K. M. A. Islam, Physical properties and defect processes of M_3SnC_2 (M =Ti, Zr, Hf) MAX phases: Effect of M-elements, *J. Alloys Compd.*, 2018, **748**, 804–813, DOI: **10.1016/j.jallcom.2018.03.182**.

75 H. M. Ledbetter, Elastic properties of zinc: a compilation and a review, *J. Phys. Chem. Ref. Data*, 1977, **6**(4), 1181–1203, DOI: **10.1063/1.555564**.

76 J. W. C. Met, Anisotropy in single-crystal refractory compounds, *J. Less-Common Met.*, 1969, **8**(316), 1969, DOI: **10.1016/0022-5088(69)90173-8**.

77 S. I. Ranganathan and M. Ostoja-Starzewski, Universal elastic anisotropy index, *Phys. Rev. Lett.*, 2008, **101**(5), 3–6, DOI: **10.1103/PhysRevLett.101.055504**.

78 C. M. Kube, Elastic anisotropy of crystals, *AIP Adv.*, 2016, **6**(9), DOI: **10.1063/1.4962996**, DOI: **10.1063/1.4962996**.

79 J. Wang, Y. Zhou, T. Liao and Z. Lin, First-principles prediction of low shear-strain resistance of Al_3BC_3: a metal borocarbide containing short linear BC2 units, *Appl. Phys. Lett.*, 2006, **89**(2), 2012–2015, DOI: **10.1063/1.2220549**.

80 G. D. Healy, AnisoVis, GitHub - DaveHealy-github_AnisoVis_Visualisation of Anisotropy, 2021, **https://github.com/DaveHealy-Aberdeen/AnisoVis**.

81 R. Gaillac, P. Pullumbi and F. X. Coudert, ELATE: an open-source online application for analysis and visualization of elastic tensors, *J. Phys.: Condens. Matter*, 2016, **28**(27), 275201, DOI: **10.1088/0953-8984/28/27/275201**.

82 M. W. Qureshi, M. A. Ali and X. Ma, Screen the thermomechanical and optical properties of the new ductile 314 MAX phase boride Zr_3CdB_4: a DFT insight, *J. Alloys Compd.*, 2021, **877**, 160248.

83 Y. Zhou and Z. Sun, Electronic structure and bonding properties of layered machinable and ceramics, *Phys. Rev. B: Condens. Matter Mater. Phys.*, 2000, **61**(19), 12570–12573, DOI: **10.1103/PhysRevB.61.12570**.

84 N. A. Shahed, M. Nishat, S. Khanom, M. K. Hossain, M. A. Hossain and F. Ahmed, Effect of oxygen deficiency on optical and magnetic properties of Ba_2MMoO_6 (M=Cr, Mn, Fe): a first-principles study, *Comput. Condens. Matter*, 2020, **23**, e00464.

85 N. A. Shahed, M. K. Hossain, S. Khanom, M. Nishat, M. J. Alam, M. A. Hossain and F. Ahmed, Optical and magnetic properties of oxygen-deficient Ba_2 Mn, Fe and μ $MMoO_6$ μ (M = =0, 0.5, 1.0) in a monoclinic phase: a first-principles study, *Spin*, 2020, **10**(3), 1–9, DOI: **10.1142/S201032472050023X**.

86 I. Salama and M. W. Barsoum, S ynthesis and mechanical properties of Nb_2 AlC and $(Ti, Nb)_2$ AlC, *J. Alloys Compd.*, 2002, **347**, 271–278.

87 A. J. Stone and D. J. Wales, Theoretical studies of icosahedral C, and some fuzlated species, *Chem. Phys. Lett.*, 1986, **128**(5), 501–503.

88 M. D. Segall, R. Shah, C. J. Pickard and M. C. Payne, Population analysis of plane-wave electronic structure calculations of bulk materials, *Phys. Rev. B: Condens. Matter Mater. Phys.*, 2013, **54**(23), 317–320, DOI: **10.1103/physrevb.54.16317**.

89 F. Wooten, Optical properties of solids, *Sol. Energy Mater.*, 1989, **18**(3–4), 231, DOI: **10.1016/0165-1633(89)90057-9**.

90 D. Jana, C. L. Sun, L. C. Chen and K. H. Chen, Effect of chemical doping of boron and nitrogen on the electronic, optical, and electrochemical properties of carbon nanotubes, *Prog. Mater. Sci.*, 2013, **58**(5), 565–635, DOI: **10.1016/j.pmatsci.2013.01.003**.

91 N. Korozlu, K. Colakoglu, E. Deligoz and Y. O. Ciftci, The structural, electronic and optical properties of $CdxZn_{1-X}Se$ ternary alloys, *Opt. Commun.*, 2011, **284**(7), 1863–1867, DOI: **10.1016/j.optcom.2010.11.032**.

92 M. Yang, B. Chang, G. Hao, J. Guo, H. Wang and M. Wang, Comparison of optical properties between Wurtzite and zinc-blende $Ga_{0.75}Al_{0.25}N$, *Optik*, 2014, **125**(1), 424–427, DOI: **10.1016/j.ijleo.2013.06.083**.

93 Q. J. Liu, N. C. Zhang, F. S. Liu, H. Y. Wang and Z. T. Liu, $BaTiO_3$: Energy, geometrical and electronic structure, relationship between optical constant and density from f irst-principles calculations, *Opt. Mater.*, 2013, **35**(12), 2629–2637, DOI: **10.1016/j.optmat.2013.07.034**.

94 R. Saniz, L. H. Ye, T. Shishidou and A. J. Freeman, Structural, electronic, and optical properties of $NiAl_3$: first-principles calculations, *Phys. Rev. B: Condens. Matter Mater. Phys.*, 2006, **74**(1), 5–11, DOI: **10.1103/PhysRevB.74.014209**.

95 R. Philip, Photonic crystal fibers, *Science*, 2003, **299**(5605), 358–362, DOI: **10.1126/science.1078550**.

96 L. Bellaiche and D. Vanderbilt, Virtual crystal approximation revisited: Application to dielectric and piezoelectric properties of perovskites, *Phys. Rev. B: Condens. Matter Mater. Phys.*, 2000, **61**(12), 7877–7882, DOI: **10.1103/PhysRevB.61.7877**.

97 M. Nishat, M. K. Hossain, M. R. Hossain, S. Khanom, F. Ahmed and M. A. Hossain, Role of metal and anions in organo-metal halide perovskites $CH_3NH_3MX_3$ (M: Cu, Zn, Ga, Ge, Sn, Pb; X: Cl, Br, I) on structural and optoelectronic properties for photovoltaic applications, *RSC Adv.*, 2022, **12**(21), 13281–13294, DOI: **10.1039/d1ra08561a**.

98 S. Li, R. Ahuja, M. W. Barsoum, P. Jena and B. Johansson, Optical properties of Ti_3 and Ti_4AlN_3SiC, *Appl. Phys. Lett.*, 2008, **92**(22), 90–93, DOI: **10.1063/1.2938862**.

99 X. Ming, S. Wang, Y. Gang, J. Li, Y. Zheng, L. Chen, *et al.*, Optical properties of cubic Ti_3N_4, Zr_3N_4, and Hf_3N_4, *Appl. Phys. Lett.*, 2006, **89**(15), 151908.

100 J. S. De Almeida and R. Ahuja, Electronic and optical properties of RuO_2 and IrO_2, *Phys. Rev. B: Condens. Matter Mater. Phys.*, 2006, **73**(16), 1–6, DOI: **10.1103/PhysRevB.73.165102**.

101 O. L. Anderson, A simplified method for calculating the, *J. Phys. Chem. Solids*, 1963, **24**, 909–917.

102 E. Schreiber, O. L. Anderson, and N. Soga, *Elastic Constants and Their Measurement*, McGraw-Hill, New York, 1973, vol. 6.

103 D. R. Clarke, Materials selections guidelines for low thermal conductivity thermal barrier coatings, *Surf. Coat. Technol.*, 2003, **163–164**, 67–74, DOI: **10.1016/S02578972(02)00593-5**.

104 Y. Liu, V. R. Cooper, B. Wang, H. Xiang, Q. Li, Y. Gao, J. Yang, Y. Zhou and B. Liu, *Mater. Res. Lett.*, 2019, **7**, 145–151.

105 M. E. Fine, L. D. Brown and H. L. Marcus, Elastic constants versus melting temperature in metals, *Scr. Metall.*, 1984, **18**(9), 951–956, DOI: **10.1016/0036-9748(84)90267-9**.